Earth's Future

RESEARCH ARTICLE
10.1029/2020EF001520

Key Points:
- Top-down emissions from several recent studies are within the range of bottom-up inventories and exhibit a similar level of uncertainty for some regions and species
- In China, the United States, and Europe emission trends in the last decade from SSP126 match most closely actual trends from bottom-up and top-down estimates
- In Western Africa and India recent emission trends from low pollution control scenarios (SSP460 and SSP370, respectively) match most closely actual trends

Supporting Information:
- Supporting Information S1

Correspondence to:
N. Elguindi,
elgn@aero.obs-mip.fr

Citation:
Elguindi, N., Granier, C., Stavrakou, T., Darras, S., Bauwens, M., Cao, H., et al. (2020). Intercomparison of magnitudes and trends in anthropogenic surface emissions from bottom-up inventories, top-down estimates, and emission scenarios. *Earth's Future*, *8*, e2020EF001520. https://doi.org/10.1029/2020EF001520

Received 13 FEB 2020
Accepted 31 MAY 2020
Accepted article online 10 JUN 2020

Intercomparison of Magnitudes and Trends in Anthropogenic Surface Emissions From Bottom-Up Inventories, Top-Down Estimates, and Emission Scenarios

N. Elguindi[1], C. Granier[1,2], T. Stavrakou[3], S. Darras[4], M. Bauwens[3], H. Cao[5], C. Chen[6,7], H. A. C. Denier van der Gon[8], O. Dubovik[6], T. M. Fu[9], D. K. Henze[10], Z. Jiang[11], S. Keita[12,13], J. J. P. Kuenen[8], J. Kurokawa[14], C. Liousse[1], K. Miyazaki[15], J.-F. Müller[3], Z. Qu[10,16], F. Solmon[1], and B. Zheng[17]

[1]Laboratoire d'Aérologie, CNRS, Université de Toulouse, Toulouse, France, [2]NOAA/ESRL/CSD-CIRES, University of Colorado, Boulder, CO, USA, [3]Division of Atmospheric Composition, Royal Belgian Institute for Space Aeronomy, Brussels, Belgium, [4]Observatoire Midi-Pyrénées, Toulouse, France, [5]Department of Mechanical Engineering (ME), University of Colorado Boulder, Boulder, CO, USA, [6]Laboratoire d'Optique Atmosphérique (LOA), UMR8518 CNRS, Université de Lille, Lille, France, [7]GRASP-SAS, Remote Sensing Developments, Université de Lille, Lille, France, [8]Department of Climate, Air and Sustainability, TNO, Utrecht, The Netherlands, [9]School of Environmental Science and Engineering, Southern University of Science and Technology, Shenzhen, China, [10]Department of Mechanical Engineering, University of Colorado Boulder, Boulder, CO, USA, [11]School of Earth and Space Sciences, University of Science and Technology of China, Hefei, China, [12]UFR sciences Biologiques, University PGC, Korhogo, Côte d'Ivoire, [13]Laboratoire de Physique de l'Atmosphère (LAPA-UFHB), University PGC, Korhogo, Côte d'Ivoire, [14]Asia Center for Air Pollution Research, Niigata, Japan, [15]Jet Propulsion Laboratory, California Institute of Technology, Pasadena, CA, USA, [16]John A. Paulson School of Engineering and Applied Science, Harvard University, Cambridge, MA, USA, [17]Laboratoire des Sciences du Climat et de l'Environnement, CEA-CNRS-UVSQ, UMR8212, Gif-sur-Yvette, France

Abstract This study compares recent CO, NO_x, NMVOC, SO_2, BC, and OC anthropogenic emissions from several state-of-the-art top-down estimates to global and regional bottom-up inventories and projections from five Shared Socioeconomic Pathways (SSPs) in several regions. Results show that top-down emissions derived in several recent studies exhibit similar uncertainty as bottom-up inventories in some regions for certain species and even less in the case of Chinese CO emissions. In general, the largest discrepancies are found outside of regions such as the United States, Europe, and Japan where the most accurate and detailed information on emissions is available. In some regions such as China, which has recently undergone dynamical economic growth and changes in air quality regulations, the top-down estimates better capture recent emission trends than global bottom-up inventories. These results show the potential of top-down estimates to complement bottom-up inventories and to aide in the development of emission scenarios, particularly in regions where global inventories lack the necessary up-to-date and accurate information regarding regional activity data and emission factors such as Africa and India. Areas of future work aimed at quantifying and reducing uncertainty are also highlighted. A regional comparison of recent CO and NO_x trends in the five SSPs indicate that SSP126, a strong pollution control scenario, best represents the trends from the top-down and regional bottom-up inventories in the United States, Europe, and China, while SSP460, a low-pollution control scenario, lies closest to actual trends in West Africa. This analysis can be useful for air quality forecasting and near-future pollution control/mitigation policy studies.

1. Introduction

Anthropogenic activities such as energy production, industrial processes, transportation, agriculture, and waste management are responsible for the emissions of gaseous and particulate pollutants which can both modify the climate and reduce air quality, leading to adverse impacts on the environment and human health. Accurate and up-to-date emission inventories are essential to understand the contribution of various human activities, model and predict the related changes in atmospheric composition, and design cost-effective mitigation strategies. Despite their paramount importance, large uncertainties and limitations exist in current state-of-the-art global and regional emission inventories (Crippa et al., 2018).

Based on emission estimates from inventories, along with information regarding socioeconomic, environmental, and technological trends, future emission scenarios such as the Shared Socioeconomic Pathways (SSPs) are created and used by atmospheric and chemistry models to generate future climate and pollutant concentration projections. As such, uncertainties associated with current emission estimates are directly propagated into future scenarios of emission trajectories, model climate projections, and air quality forecasts.

For a given chemical compound, emission inventories rely on the definition of key socioeconomic sectors (i.e., road traffic) involving certain technologies (i.e., car engine) characterized by specific emission factors (i.e., CO emissions per unit of fuel used per kilometer). This information is then scaled up using geographically distributed information of the corresponding activities (e.g., car traffic intensity map) to create large-scale gridded inventories. The complexity of emission modeling lies in the diversity of chemical species, as well as in the characterization and quantification of emission factors and sector activities, all of which are highly variable and influenced by socioeconomic and environmental factors. Country-level indicators used to build global emission inventories and projections often lack up-to-date regional specific information, especially in developing regions. These inventories are largely created using emission factors (EF) that are representative of conditions in developed countries, such as Europe and North America. Although often an EF is selected that represents a low technology level, the origin of the EF data is from developed countries, thereby introducing large errors and uncertainties into the emission estimates for developing countries. Furthermore, the collection of data for all countries throughout the world takes considerable time; by the time the inventories are updated, there is thus often a significant lag from the present day.

Alternatively, inverse modeling techniques, which constrain atmospheric models by observations to estimate surface emissions, have been used to derive emissions for various air pollutants (e.g., Arellano et al., 2004; Miyazaki et al., 2017; Müller & Stavrakou, 2005; Stavrakou et al., 2012). A main advantage of these estimation techniques is their high spatial coverage, in particular, when spaceborne atmospheric data are used as constraints. Another benefit is that they can provide more timely emission estimates than traditional bottom-up inventories, which are generally delayed by a few years. Inverse modeling has the potential to reduce uncertainty in air quality and chemistry climate models by providing more constrained emission data, especially in regions of the world where bottom-up estimates are believed to be deficient. Nevertheless, top-down estimates have limitations and uncertainties as well. Notably, uncertainties are associated with the use of atmospheric models, in particular, their representation of transport and chemical processes (e.g. Jiang et al., 2013; Stavrakou et al., 2013). Another source of uncertainties is related to the observations used to constrain the models. For example, satellite data intercomparison studies revealed large differences between different retrievals of the same compound as well as significant biases against well-calibrated validation data, reaching up to a factor of 1.6 in the case of HCHO (Zhu et al., 2016). Studies have also reported differences of around 40% for NO_x (Lorente et al., 2017) and up to 13% for CO (George et al., 2015). Streets et al. (2013) suggests that top-down emissions could be used to provide timely updates to emission trends and intra-annual temporal variations. However, before they can be used to supplement bottom-up emission inventories, an assessment of their reliability and associated uncertainty over diverse regions is needed.

The main goal of this study is to provide an intercomparison of top-down emission magnitudes and trends derived from inverse modeling techniques for various species (CO, NO_x, NMVOC, SO_2, BC, and OC) for several regions of the world. Specifically, we evaluate the magnitude and range of top-down emissions within the context of current state-of-the-art bottom-up global and regional emission inventories. Similarly, the trends for the different regions are also evaluated. To this end, we compiled estimates of anthropogenic emissions from 12 different sources based on various inverse methods. These estimates are compared to the most widely used global inventories EDGARv4.3.2 (Crippa et al., 2018) and CEDS (Hosley et al., 2018), as well as to recent regional inventories for Europe (CAMS-REG-AP, Granier et al., 2019), Africa (DACCIWA, https://www.eccad3.sedoo.fr), and China (MEICv1.3: http://www.meicmodel.org, Zheng, Tong, Li et al., 2018). While it is important to evaluate the potential for top-down emissions to provide valuable information regarding intra-annual variability, this study focuses exclusively on annual emission totals and interannual trends.

Another objective is to compare the trends in the projected emissions of the Shared Socioeconomic Pathways (SSPs) developed for the sixth Climate Model Intercomparison Project (CMIP6) (Kriegler et al., 2014; Riahi et al., 2017) to the current best estimates of emission trends for the recent past in selected regions. We aim to

Table 1
Description of Inverse Modeling Estimates Considered in This Study

	Species	Region	Res. (lon × lat)	Period	CTM	Satellite constraint	Inversion method
Global							
Chen et al. (2019)	OC, BC	Global	2.5° × 2°	2006–2011	GEOS-Chem	PARASOL/GRASP* AOD/AAOD	Adjoint
TCR-2	NO_x	Global	1.125° × 1.125°	2005–2018	MIROC-Chem	OMI/GOME-2/SCIAMACHY NO_2,TES O_3, MOPITT CO, MLS O_3/HNO_3	Ensemble Kalman filter
TCR-2	SO_2	Global	1.125° × 1.125°	2005–2018	MIROC-Chem	OMI/GOME-2/SCIAMACHY NO_2, OMI SO_2, TES O_3, MOPITT CO, MLS O_3/HNO_3	Ensemble Kalman filter
Müller (2018)	CO	Global	2.5° × 2°	2013	IMAGESv2	IASI CO and OH levels based on methylchloroform (MCF) obs.	Adjoint
Zheng et al. (2019)	CO	Global	3.75° × 1.9°	2000–2017	LMDz-SACS	MOPITT CO, OMI HCHO, GOSAT XCH_4	Bayesian
Jiang et al. (2017)	CO	Global	5° × 4°	2001–2015	GEOS-Chem	MOPITT CO and OH levels based on MCF obs.	Adjoint
Qu et al. (2020)	NO_x	Global	2.5° × 2°	2005–2016	GEOS-Chem	OMI NO_2	Adjoint
Regional							
Cao et al. (2018)	NMVOC	China	5° × 4°	2007	GEOS-Chem	GOME-2/OMI HCHO/ CHOCHO	Adjoint
Qu, Henze, Theys, et al. (2019)	NO_x, SO_2	East Asia	0.5° × 0.667°	2005–2012	GEOS-Chem	OMI SO_2, NO_2	Adjoint
Qu, Henze, Li, et al. (2019)	SO_2	East Asia	2.5° × 2°	2005–2017	GEOS-Chem	OMI SO_2	Adjoint
Stavrakou et al. (2017)	NMVOC	China	2.5° × 2°	2005–2014	IMAGESv2	OMI HCHO	Adjoint

evaluate which narrative describes best the direction taken by the different regions in terms of emissions. Assessing how well the scenarios capture recent emission trends will be useful for determining their suitability for studies that evaluate emissions in the recent past and near future, such as pollution control/mitigation impact studies and air quality forecasting. Furthermore, we compare CO and NO_x emissions from the SSPs to those of the Representative Concentration Pathways (RCPs) that were used in the fifth Climate Model Intercomparison Project (CMIP5) (Moss et al., 2010; van Vuuren et al., 2011) for several world regions. While a comprehensive overview of the SSP emissions and comparison with the RCPs is presented in Gidden et al. (2019), we are focused on the regional scale and intend to aid in the interpretation and analysis of regional climate change studies.

2. Materials and Methods

This study compares 12 different top-down emission estimates to several state-of-the-art global and regional bottom-up inventories for CO, NO_x, NMVOC, SO_2, OC, and BC. A description of each of the top-down estimates is provided below. Details and references for each of the top-down and bottom-up inventories are also given in Tables 1 and 2, respectively. We focus on the following 12 regions as defined by the IMAGE 2.4 26 regions (Bouwman et al., 2006): China, the Middle East, Western Africa, the United States, Western and Central Europe, South America, India+, Southeast Asia, Indonesia+, Oceania, and Southern Africa. Note that India+ includes neighboring countries such as Pakistan, Afghanistan, Nepal, and Bangladesh. A map of the regions is shown in the supporting information (Figure S1). These regions were selected based on their economic and geographic diversity, as well as on the availability of top-down and bottom-up regional inventories. The regional averages for all datasets are calculated on their native grids.

2.1. Calculation of Trends and Percent Differences

We evaluate recent trends in emissions from the five SSPs based on the years 2010–2020. The trends are derived from ordinary linear regression and expressed in units of percent change per year relative to the mean over the data period. The SSP trends are compared to trends which are based on the emissions from the inventories and inversion estimates. These trend estimates are calculated by averaging the trends from all available inventories for a particular region, including all inverse modeling estimates and bottom-up inventories which are available from 2010 until at least 2015 which are statistically significant ($p > 0.05$).

Table 2
Description of Global and Regional Bottom-Up Inventories Considered in This Study

	Species	Region	Res. (lon × lat)	Period	Reference
Global inventories					
CAMS-GLOB-ANT	NO_x, CO, NMVOC, SO_2, OC, BC	Global	0.1° × 0.1°	2000–2019	Elguindi et al. (2020), Granier et al. (2019)
EDGARv4.3.	NO_x, CO, NMVOC, SO_2, OC, BC	Global	0.1° × 0.1°	1970–2012	Crippa et al. (2018)
CEDS	NO_x, CO, NMVOC, SO_2, OC, BC	Global	0.5° × 0.5°	1950–2014	Hosley et al. (2018)
HTAPv2	NO_x, CO, NMVOC, SO_2, OC, BC	Global	0.1° × 0.1°	2008, 2010	Janssens-Maenhout et al. (2015)
MACCity	NO_x, CO, NMVOC, SO_2, OC, BC	Global	0.5° × 0.5°	2007	Granier et al. (2011)
Regional inventories					
CAMS-REG-AP	NO_x, CO, NMVOC, SO_2, OC, BC	Europe	0.1° × 0.05°	2000–2017	Kuenen et al. (2014), Granier et al. (2019)
DACCIWA	NO_x, CO, NMVOC, SO_2, OC, BC	Africa	0.1° × 0.1°	2000–2015	Keita et al. (2020)
DICE-Africa	NO_x, CO, NMVOC, SO_2, OC, BC	Africa	0.1° × 0.1°	2000–2015	Marais and Wiedinmyer (2016)
US NEI	NO_x, CO, NMVOC, SO_2	USA		2000–2016	https://www.epa.gov/air-emissions-inventories
MEICv1.3	NO_x, CO, NMVOC, SO_2, OC, BC	China	0.25° × 0.25°	2008–2017	Zheng, Tong, Li et al. (2018)
REASv3.1	NO_x, CO, NMVOC, SO_2, OC, BC	Asia	0.25° × 0.25°	1950–2015	Kurokawa and Ohara (2019)
Sharma & Kumar (2016)	NO_x, CO, NMVOC, SO_2	India		2011	Sharma & Kumar (2016)
Sun et al. (2018)	NO_x, CO, NMVOC, SO_2	China		1949–2015	Sun et al. (2018)

A list of the individual trends is provided in the supporting information. Note that MACCity and CAMS-GLOB-ANT are excluded because their recent years are based on projections of past trends from inventories and are therefore not considered independent. Unless otherwise specified, percentage differences in the range of emission estimates are calculated based on the average between the highest and lowest values.

3. Data

3.1. Top-Down Emissions

3.1.1. Global

Chen et al. (2019)

Global daily carbonaceous aerosol (OC and BC) emissions for the period 2006–2011 are derived using the GEOS-Chem adjoint model (Henze et al., 2007) at a spatial resolution of 2.5° × 2° (Chen et al., 2019). OC and BC emission sources are constrained using retrievals of aerosol optical depth (AOD) and aerosol absorption optical depth (AAOD) (Chen et al., 2018, 2019) from the multi-angular and polarimetric POLDER/PARASOL (Polarization & Anisotropy of Reflectances for Atmospheric Sciences coupled with Observations from a Lidar) measurements retrieved via the GRASP (General Retrieval of Atmosphere and Surface Properties) algorithm (www.grasp-open.com) (Dubovik et al., 2011, 2014). Note that the anthropogenic contribution of the total derived black and organic carbon emissions is estimated based on a ratio which is applied in the GEOS-Chem (v10-1) model.

Jiang et al. (2017)

Global CO emissions are constrained over the period 2001–2015 by assimilating multispectral CO measurements from MOPITT (version 6) using the 4D-Var data assimilation system (adjoint) in the GEOS-Chem model at a spatial resolution of 5° × 4°. The initial conditions and land boundary conditions (CO concentrations) are optimized using a sequential suboptimal Kalman filter. Here we include two of the inversions described in Jiang et al. (2017), one in which emissions are constrained using MOPITT CO profiles and another using total CO columns. Anthropogenic CO emissions are separated from other sources using a single scaling factor, based on the a priori emissions, to adjust all emissions in a grid.

Tropospheric Chemistry Reanalysis (TCR-2)

Global NO_x and SO_2 emissions are constrained over the period of 2005–2018 by assimilating multiple satellite data sets for multiple species (NO_2, CO, O_3, and SO_2) using the global CTM (Chemistry Transport Model) MIROC-Chem (Watanabe et al., 2011) based on the ensemble Kalman filter (EnKF) technique performed at 1.125° × 1.125° resolution in the TCR-2 framework (Miyazaki et al. 2017, 2019, 2020; Miyazaki 2020). The assimilated measurements were obtained from QA4ECV version 1.1 level 2 (L2) product for OMI (the Ozone Monitoring Instrument), GOME-2 (Global Ozone Monitoring Experiment–2), and SCIAMACHY (SCanning Imaging Absorption SpectroMeter for Atmospheric CHartography) for NO_2, TES for O_3,

MOPITT for CO, MLS for O_3 and HNO_3, and OMI for SO_2. Anthropogenic and natural emissions are separated by using a correction scheme described in Miyazaki et al. (2017).

Müller (2018)

Global CO emissions for 2013 are derived at 2° × 2.5° resolution based on the adjoint of the IMAGESv2 model constrained by satellite IASI CO column data. The model uses prescribed OH fields constrained by methylchloroform measurements. An ensemble of top-down simulations is carried out, and the top-down emissions are compared with various independent CO observations and evaluated. The inversion adopting the lowest average OH level in the Northern Hemisphere provides the best agreement with all tested independent observation data sets, and the corresponding top-down emissions are used in our study. Emissions are derived for three categories (anthropogenic, biogenic, and biomass burning) using a technique which relies on the spatiotemporal patterns of the a priori emissions, through assumed correlations between a priori emission errors. In essence, the inversion tries to preserve the patterns of the a priori. The strength of that constraint is determined by the assumed correlations.

Zheng et al. (2019)

Global CO emissions for the period 2000–2017 are derived using the global 3-D transport model of the Laboratoire de Météorologie Dynamique (LMDz) coupled with a simplified chemistry module, Simplified Atmospheric Chemistry assimilation System (SACS) based on a multi-species atmospheric Bayesian inversion approach (Zheng, Chevallier et al., 2018) at a spatial resolution of 3.75° × 1.9°. Zheng et al. (2019) perform the following three global inversions which are used in this study: (i) an inversion constrained only by CO total column data from the MOPITT version 7 over 2000–2017 (inversion 1); (ii) an inversion also constrained by HCHO column data from Ozone Monitoring Instrument (OMI) version 3 on the basis of inversion 1 for the period 2005–2017 (inversion 2); (iii) an inversion further constrained by column-averaged dry air mole fractions of CH_4 (XCH_4) from Greenhouse gases Observing SATellite (GOSAT) on the basis of inversion 2 for the period 2010–2017 (inversion 3). Emissions are derived for four categories (anthropogenic, biomass burning, biogenic, and oceanic) by multiplying the optimized eight daily surface CO total fluxes by the proportion of each sector in each model grid cell as given by the prior.

Qu et al. (2020)

Global NO_x emissions for the period 2005–2016 are derived using the GEOS-Chem adjoint model (Henze, 2009; Henze et al., 2007) and a hybrid 4D-Var/mass balance approach at a 2° × 2.5° horizontal resolution. In order to assess the uncertainty related to satellite retrievals, two inversions are performed using different OMI satellite retrievals to constrain the emissions: the NASAv3 standard product OMNO2 (Krotkov et al., 2017) and DOMINOv2 from KNMI (Boersma et al., 2011). These inversions are referred to as Qu-NASA and Qu-DOMINO.

3.1.2. Regional

Cao et al. (2018)

NMVOC emissions in China for the year 2007 are derived using the GEOS-Chem CTM (version 8.2.1) and its adjoint at a spatial resolution of 5° × 4°). The GEOS-Chem CTM was updated to include improved NMVOC chemical schemes. Emissions are constrained by using HCHO and glyoxal columns observed by the GOME-2A and OMI satellite instruments. Four inversion experiments using different combinations of these satellite observations were conducted in order to explore their impacts on the top-down emission estimates. The anthropogenic NMVOC emission estimates for 2007 range from 16.4 to 23.6 Tg yr^{-1}. In this study, we show the average of the four estimates which is 20.2 Tg yr^{-1}.

Qu, Henze, Theys et al. (2019)

NO_x and SO_2 emissions in East Asia for the period 2005–2012 are derived simultaneously using the GEOS-Chem adjoint model (Henze, 2009; Henze et al., 2007) and a hybrid 4D-Var/mass balance approach at 0.5° × 0.667° resolution (Qu et al., 2017). The emissions are constrained by the OMI NO_2 NASA standard product (Krotkov et al., 2017) and the OMI Royal Belgian Institute for Space Aeronomy (BIRA) SO_2 product (Theys et al., 2015). We refer to this inventory as Qu-joint. An inversion is also performed constraining only NO_2 in order to assess the benefits of constraining multiple species. This inversion is referred to as Qu-single. In order to estimate the anthropogenic contribution of NO_x emissions, natural sources (e.g., biomass burning, soil, and lightening) estimated from bottom-up inventories used in the GEOS-Chem model have been subtracted from the total annual budget. The inversions were performed on a limited domain which does

not included all of the countries of the India+ region shown in Figure S1; therefore, the averages for Qu-single and Qu-joint are for India only.

Qu, Henze, Li et al. (2019)

Global SO_2 emissions for the period 2005–2017 are derived using the GEOS-Chem adjoint model (Henze, 2009; Henze et al., 2007) and a hybrid 4D-Var/mass balance approach at a 2° × 2.5° horizontal resolution. In order to assess the uncertainty related to satellite retrievals, two inversions are performed using different OMI satellite retrievals to constrain the emissions: the NASA standard product OMSO2 (Li et al., 2013) and the BIRA product (Theys et al., 2015). Note that these SO_2 emissions are shown only for China and India because the estimates are less accurate in comparatively cleaner areas with lower SO2 columns due to negative column densities in the OMI SO_2 retrievals (Qu et al., 2019). These inversions are referred to as Qu-BIRA and Qu-NASA.

Stavrakou et al. (2017)

Global NMVOC emissions for the period 2005–2014 are derived using the adjoint model technique in the IMAGESv2 global CTM at a spatial resolution of 2° × 2.5°. Emissions from open fire vegetation and human activities are constrained using vertical columns of formaldehyde (HCHO) retrieved from the Ozone Monitoring Instrument (OMI-BIRA). The anthropogenic VOC sources are found to be weakly constrained by the inversions due to their small contribution to the total HCHO columns (Stavrakou et al., 2009), except over strongly polluted regions. Therefore, we only consider NMVOC inversion results for China.

3.2. Bottom-Up Emissions

In this study, we compare 13 of the most recent surface anthropogenic global and regional bottom-up inventories. Included in the global inventories are EDGARv4.3.2 (JRC, Crippa et al., 2018) and CEDS (Hosley et al., 2018) which are both traditional bottom-up inventories. We also compare CAMS-GLOB-ANTv4.1 and MACCity which are based on bottom-up inventories and projections, thereby provide emissions to the current year. The CAMS global emissions are based on both the EDGARv4.3.2 and CEDS emissions. The standard version of CAMS-GLOB-ANT (version 4.1) used in this study applies the monthly profiles provided by CAMS-GLOB-TEMPO (Granier et al., 2019) to the annual emissions from EDGARv4.3.2 for the years 2000–2012. After 2012, the data are linearly extrapolated to 2020 using trends derived from the CEDS emissions for the years 2011–2014. A detailed description of all the global and regional bottom-up inventories are presented in the Supplement, along with a brief discussion regarding the uncertainties among global inventories.

3.3. Shared Socioeconomic Pathways (SSPs)

The projected emissions from five SSPs were developed for use in the current Coupled Model Intercomparison Project phase 6 (Eyring et al., 2016). The SSPs are global scenarios which describe how the future emissions might evolve according to socioeconomic development, demographics, technological advances within the context of climate change mitigation and adaptation during the period 2015–2100 (O'Neill et al., 2014; van Vuuren et al., 2014). The air pollutant emission trajectories associated with the SSP scenarios have been harmonized with the CEDS historical global inventory for the year 2015 and are described in Rao et al. (2017) and Gidden et al. (2019). The pathways are based on five narratives describing alternative socioeconomic developments. SSP1 and SSP5 assume strong pollution control scenarios and therefore emissions which are substantially lower than current levels, whereas according to SSP3 and SSP4, future emissions are higher than current levels. SSP2 is based on a medium pollution control scenario where emissions remain close to current levels (Rao et al., 2017). In addition, mitigation policies are added to each scenario in order to achieve a prescribed radiative forcing by the end of the 21st century (i.e., 2.6, 4.5, 6.0, and 8.5 W m^{-2}).

In this study, we focus on the four Tier 1 SSPs (SSP126, SSP245, SSP370, and SSP585), which have the same radiative forcing as the RCPs used in CMIP5, but combine socioeconomic and technological developments, and have been given priority in CMIP6 (O'Neill et al., 2016). In addition, we also analyze SSP460, which has been designated as a Tier 2 scenario in order to complement and extend the Tier 1 scenarios and the RCPs (O'Neill et al., 2016). The emissions associated with these scenarios are available at a 0.5° × 0.5° spatial resolution (https://esgf-node.llnl.gov/projects/input4mips).

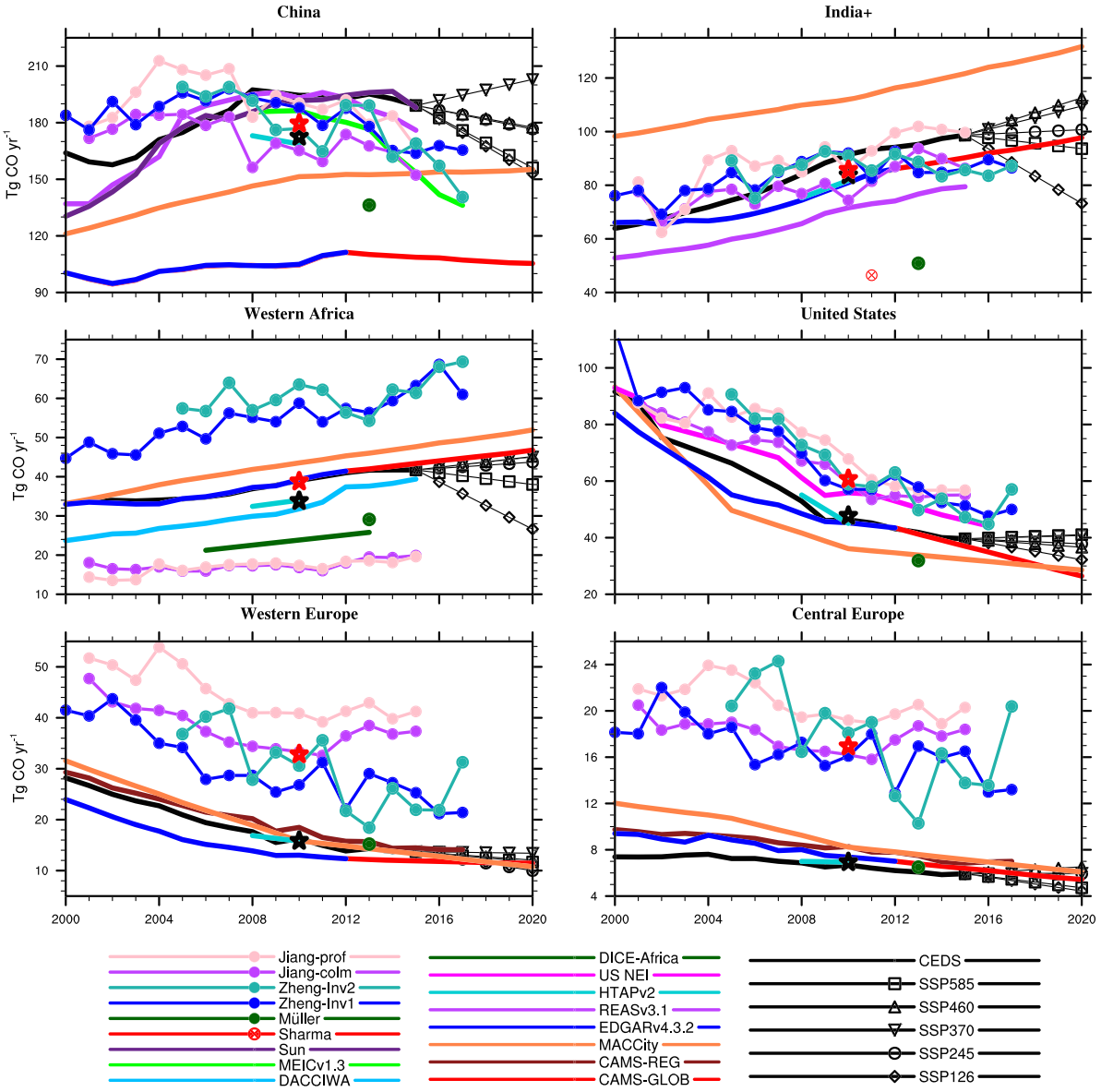

Figure 1. CO emissions from bottom-up (BU) and top-down (TD) inventories and the SSPs. Ensemble means for the year 2010 are denoted by black (BU) and red (TD) stars as given in Table 3. Note that the Sharma estimate is for the national boundaries of India only. BU 2010 mean excludes MACCity.

4. Comparison of Emission Inventories and Inverse Modeling Estimates

In this section, we compare top-down anthropogenic emission estimates of CO, NO_x, NMVOC, SO_2, BC, and OC to global and regional inventories which were developed using bottom-up estimation methods over the six regions of interest described in section 2 and shown in Figure 1. Note that while the bottom-up inventories only consider anthropogenic sources, the top-down inventories use various methods to separate anthropogenic and natural emissions (see section 3.1 and references therein for details) which introduces an additional source of uncertainty. In order to provide a quantitative overview on emission totals and uncertainty, the ensemble mean, min, and max bottom-up emissions for the year 2010 for each region and species are provided in Table 3. The annual timeseries of the top-down and bottom-up inventories are presented in Figures 2–4.

Table 3
Annual mean emissions (Tg) for the bottom-up (BU) and top-down (TD) inventory ensemble mean, minimum, and maximum for the year 2010

		CO	NO_x	NMVOC	SO_2	BC	OC
CN	BU_mean	173.2 (52%)	19.0 (52%)	25.3 (16%)	25.3 (78%)	1.80 (59%)	3.44 (55%)
	BU_min	104.9 (*Edgar*)	15.6 (*Edgar*)	22.9 (*HTAP*)	15.7 (*Sun*)	1.28 (*Edgar*)	2.78 (*Edgar*)
	BU_max	194.5 (*CEDS*)	25.4 (*MEIC*)	27.0 (*CEDS*)	35.5 (*CEDS*)	2.34 (*CEDS*)	4.66 (*CEDS*)
	TD_mean	180.1 (8%)	20.6 (61%)	26.1 (—)	20.5 (%)	1.29 (—)	4.12 (—)
	TD_min	165.2 (*J-colm*)	16.8 (*Q-sing*)	26.1 (Stavrak)	17.1 (*TCR-2*)	1.29 (*Chen*)	4.12 (*Chen*)
	TD_max	190.3 (*J-prof*)	29.3 (*Q-DOM*)	26.1 (Stavrak)	24.2 (*Qu-bira*)	1.29 (*Chen*)	4.12 (*Chen*)
IN	BU_mean	83.7 (24%)	7.5 (59%)	18.3 (42%)	11.8 (27%)	1.00 (50%)	2.85 (27%)
	BU_min	71.4 (*REAS*)	6.0 (*REAS*)	14.6 (*Edgar*)	10.7 (*Edgar*)	0.71 (*Edgar*)	2.05 (*Edgar*)
	BU_max	91.4 (*CEDS*)	10.4 (*CEDS*)	22.3 (*CEDS*)	13.9 (*CEDS*)	1.21 (*HTAP*)	3.67 (*CEDS*)
	TD_mean	86.0 (20%)	7.7 (69%)		5.1 (%)	0.56 (—)	3.31 (—)
	TD_min	74.4 (*J-colm*)	5.4 (*Q-sing*)	—	4.1 (*TCR-2*)	0.56 (*Chen*)	3.31 (*Chen*)
	TD_max	92.0 (*Z-Inv1*)	10.7 (*Q-DOM*)		6.2 (*Qu-bira*)	0.56 (*Chen*)	3.31 (*Chen*)
WA	BU_mean	34.0 (45%)	1.0 (60%)	11.2 (76%)	0.4 (75%)	0.50 (50%)	1.76 (100%)
	BU_min	23.8 (*HTAP*)	0.7 (*HTAP*)	5.5 (*DACCI*)	0.2 (*DACCI*)	0.35 (*Edgar*)	1.07 (*Edgar*)
	BU_max	39.2 (*Edgar*)	1.3 (*DACCI*)	14 (*HTAP*)	0.5 (*Edgar*)	0.60 (*CEDS*)	2.83 (*DACCI*)
	TD_mean	39.1 (119%)	1.0 (90%)			0.34 (—)	4.67 (—)
	TD_min	16.8 (*J-colm*)	0.6 (*Q-NASA*)	—	—	0.34 (*Chen*)	4.67 (*Chen*)
	TD_max	63.5 (*Z-Inv2*)	1.5 (*Q-DOM*)			0.34 (*Chen*)	4.67 (*Chen*)
US	BU_mean	48.2 (22%)	8.5 (11%)	12.5 (17%)	8.0 (38%)	0.24 (33%)	0.37 (54%)
	BU_min	45.1 (HTAP)	7.9 (*Edgar*)	11.5 (*CEDS*)	7.0 (*EPA*)	0.22 (*Edgar*)	0.26 (*Edgar*)
	BU_max	55.9 (*EPA*)	8.8 (*EPA*)	13.6 (*EPA*)	10.0 (*HTAP*)	0.29 (*HTAP*)	0.46 (*HTAP*)
	TD_mean	60.7 (18%)	9.7 (41%)			0.53 (—)	0.76 (—)
	TD_min	57.1 (*Z-Inv1*)	8.9 (*TCR-2*)	—	—	0.53 (*Chen*)	0.76 (*Chen*)
	TD_max	67.8 (*J-prof*)	12.9 (*Q-DOM*)			0.53 (*Chen*)	0.76 (*Chen*)
WE	BU_mean	15.9 (35%)	4.7 (53%)	5.9 (37%)	2.5 (28%)	0.17 (59%)	0.31 (48%)
	BU_min	13.0 (*Edgar*)	4.1 (*Edgar*)	5.2 (*HTAP*)	2.1 (*CAMS-R*)	0.12 (*Edgar*)	0.24 (*Edgar*)
	BU_max	18.5 (*CAMS-R*)	5.5 (*CEDS*)	7.4 (*Edgar*)	2.8 (*CEDS*)	0.22 (*CEDS*)	0.39 (*CEDS*)
	TD_mean	32.9 (22%)	6.6 (58%)			0.34 (—)	0.63 (—)
	TD_min	26.8 (*Z-Inv1*)	5.0 (*Q-NASA*)	—	—	0.34 (*Chen*)	0.63 (*Chen*)
	TD_max	40.9 (*J-prof*)	8.8 (*Q-DOM*)			0.34 (*Chen*)	0.63 (*Chen*)
CE	BU_mean	7.3 (22%)	1.4 (7%)	2.0 (45%)	3.0 (17%)	0.09 (67%)	0.23 (70%)
	BU_min	6.7 (*CEDS*)	1.4 (*CAMS-R*)	1.7 (*CEDS*)	2.7 (*CAMS-R*)	0.06 (*Edgar*)	0.16 (*HTAP*)
	BU_max	8.3 (*CAMS-R*)	1.5 (*Edgar*)	2.6 (*Edgar*)	3.2 (*CEDS*)	0.12 (*CEDS*)	0.32 (*CEDS*)
	TD_mean	17.4 (18%)	1.7 (53%)			0.12 (—)	0.24 (—)
	TD_min	16.1 (*Z-Inv1*)	1.3 (*Q-NASA*)	—	—	0.12 (*Chen*)	0.24 (*Chen*)
	TD_max	19.2 (*J-prof*)	2.2 (*Q-DOM*)			0.12 (*Chen*)	0.24 (*Chen*)

Note. The percentage of the spread among the inventories relative to the ensemble mean is given in parenthesis next to the mean. NO_x is reported as NO. CE = Central Europe; CN = China, IN = India+, USA = United States, WA = Western Africa, WE = Western Europe.

4.1. CO

The annual average CO emissions for each region are displayed in Figure 1. The inversion estimates are shown for Zheng et al. (2019), Müller (2018), and Jiang et al. (2017). We compare two estimates from Zheng: Inv1 which uses satellite constraints of only columns of CO for the time period 2000–2017 and Inv2 which, in addition, is constrained by both CO and HCHO columns for 2005–2017. Two estimates from Jiang et al. (2017) are also compared: Jiang-prof which assimilates profile data and Jiang-colm which assimilates total column data. Differences between these two inversions provide a crude estimate of the uncertainty due to the model's convective transport scheme for the different regions (Jiang et al., 2013). More specific details can be found in the supporting information.

In regions with high emissions such as China, the United States, and India, the inversion estimates are generally within the range of the bottom-up inventories in terms of magnitude and have a similar range of uncertainty (105–195, 45–56, and 72–91 Tg in 2010, respectively). In all regions, Müller's estimates are significantly lower compared to those of Zheng or Jiang. The lower estimates of Müller (2018) are in part due to the use of prescribed modeled OH levels which are based on observations of methylchloroform (MCF) and further modulated based on comparisons with aircraft profiles and ground-based data. The OH field prescribed in their inversion setup is at the lower end of the range of what has been reported in

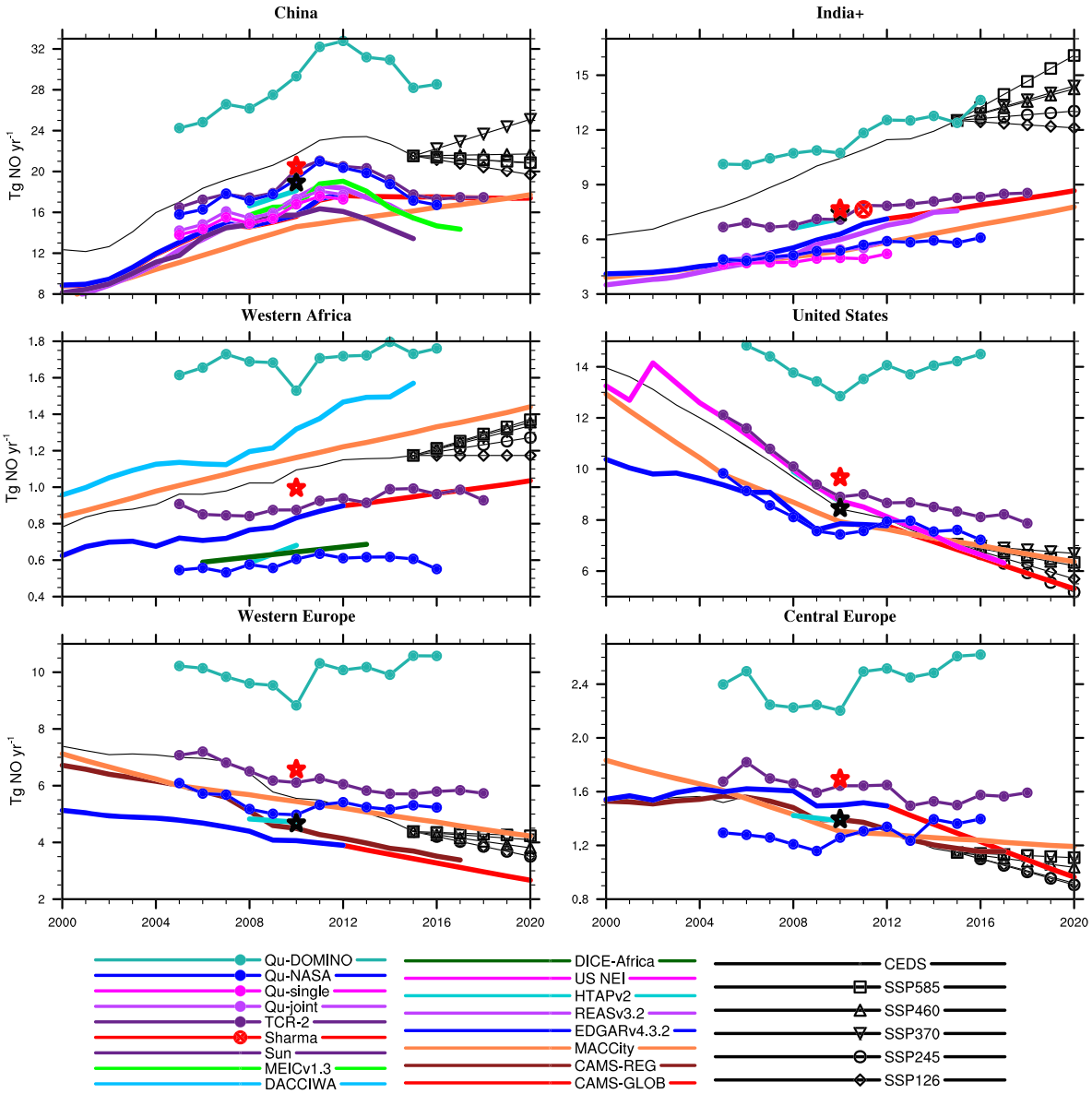

Figure 2. Same as Figure 1, except for NOx emissions.

the literature and calculated in most CTMs, implying less CO oxidation. The resulting higher CO lifetime is in turn compensated by lower optimized emissions. Another factor which could partially explain the discrepancy among the top-down estimates is the satellite data used in the inversion system. Müller assimilates IASI satellite CO data, while Zheng and Jiang, both of which have higher values, use MOPITT. George et al. (2015) have reported higher MOPITT CO total columns compared to IASI over land, in particular, for the United States and Europe, especially during boreal winter where the annual mean bias is about 35%. Its also interesting to note that the differences between the two Jiang estimates, Jiang-prof and Jiang-colm, are quite large in most regions, indicating that the convective transport schemes are a significant source of uncertainty for top-down emission estimates. For example, the difference between the two Jiang inversions in Western Europe is about 8 Tg CO in 2010 compared to the 14 Tg spread among all the top-down estimates. Assimilating profile CO data lead to higher estimates of surface emissions, particularly in regions of strong convection (Jiang et al., 2013).

In Western and Central Europe, Müller's estimate for 2013 is within the narrow range of CO emission reported by the bottom-up inventories (13–19 and 7–8 Tg in 2010, respectively) and is quite close to the

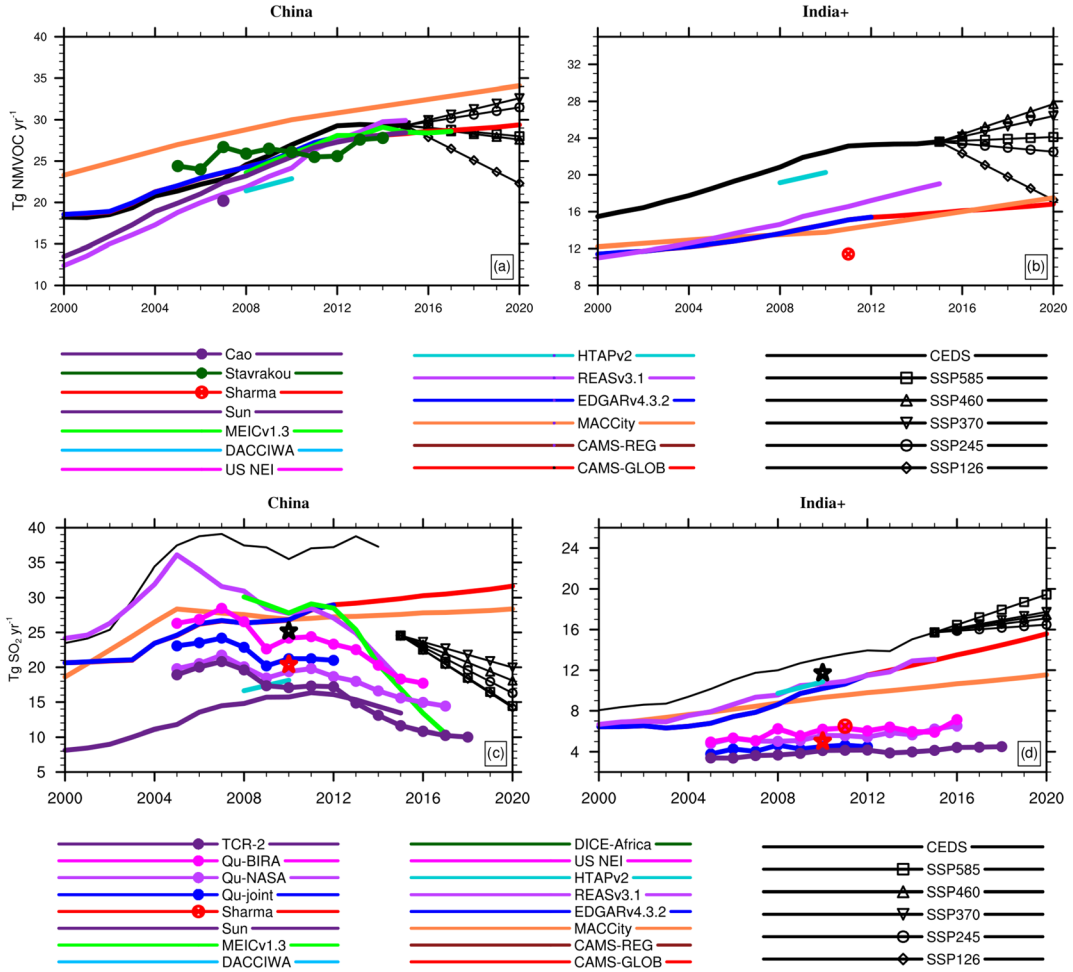

Figure 3. Same as in Figure 1, except for NMVOC (a, b) and SO2 (c,d) emissions. The NMVOC ensemble averages for China is for 2007.

regional CAMS-REG inventory (Figure 1). However, regarding the United States, Müller's estimate of CO emission is considerably below (approx. 35%) the regional U.S. EPA inventory. Müller (2018) attribute this large discrepancy to an overestimation in the U.S. bottom-up inventory, which has also been suggested in other studies (Anderson et al., 2014; Hudman et al., 2008; Jiang et al., 2015). In other regions such as China, India, and Western Africa, it is difficult to comment on the accuracy of the magnitude of the inversion (or bottom-up) emission estimates due to the lack of measurements and regional information.

The two inversion estimates of CO emissions from Zheng are quite similar in magnitude and trend in most regions, but differ in terms of interannual variability (Figure 1). The two estimates from Jiang show similar trends, but significant differences in magnitude over most regions, indicating that the type of data assimilated (e.g., profile vs. total column) has a large impact on the emission estimates. In most regions, the Jiang-prof estimates are higher than Jiang-colm. In China, there is a sharp decline in emissions after 2010 as a result of the stringent clean air policies that have been implemented in recent years due to the severe air quality issues which have been documented in other studies (Zheng, Tong, Liu et al., 2018). With the exception of the regional inventories MEICv1.3 and REASv3.1, which show a decrease of 4.4 and 2.7% yr^{-1} for the period 2011–2015, most of the inventories do not show the declining CO emissions after 2010. However, this trend is captured quite well by all of the inversion estimates which show a decrease in emissions ranging from 1 to 3% yr^{-1} over 2010–2015. While both of Zheng's estimates capture the magnitude and decreasing trend in China after 2011, Inv1 stabilizes after 2014, whereas Inv2 continues to show a declining trend similar to the MEICv1.3 emissions. Between 2011 and 2017, the Inv2 estimates decrease at an annual rate of 5.6%, while the Inv1 estimates decrease at a slower rate of 3.3%. The only difference between

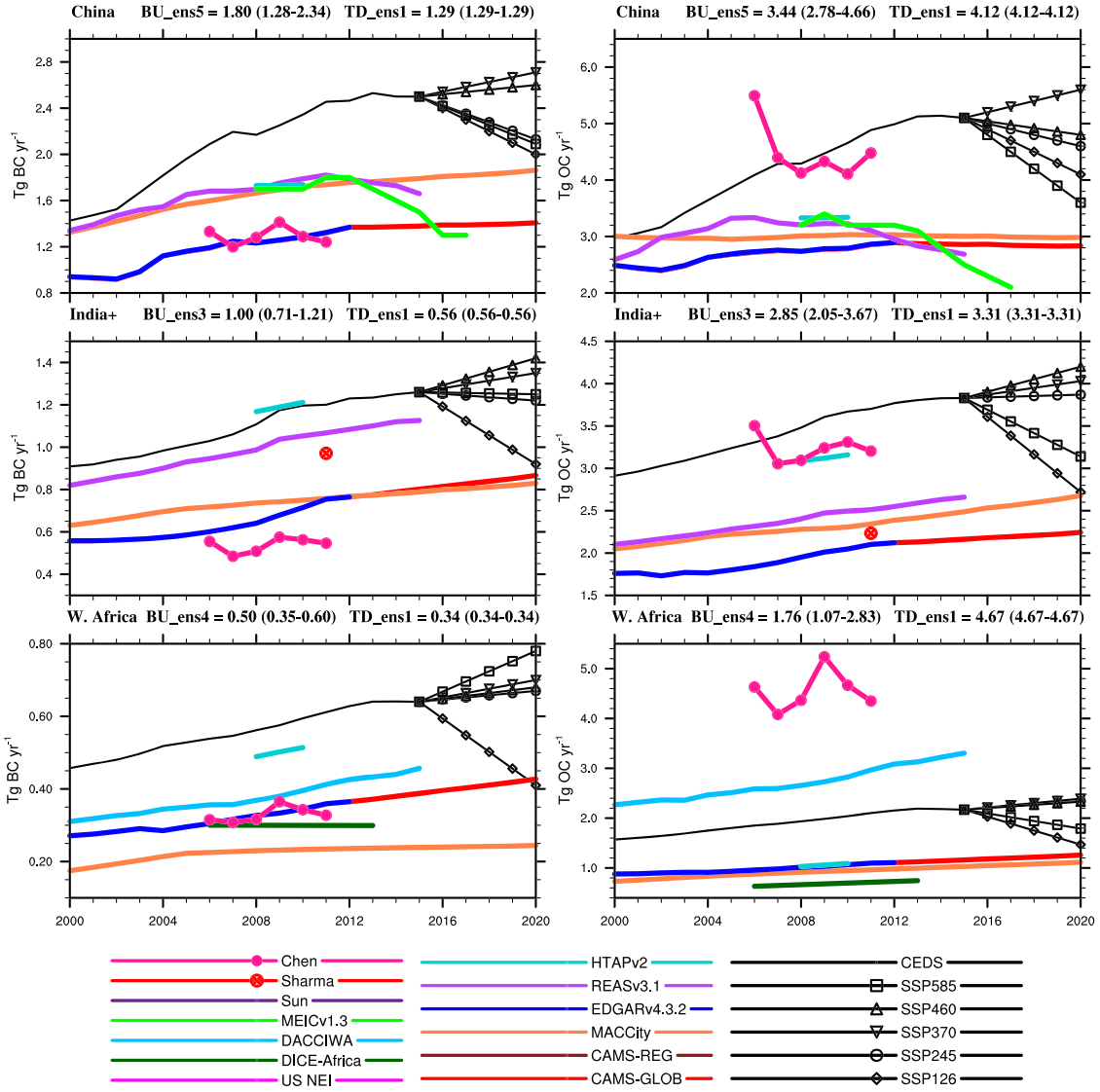

Figure 4. Same as Figure 1, except for BC and OC emissions.

these two inversions is that, in addition to constraining columns of CO, formaldehyde (HCHO) is also constrained in Inv2. Constraining HCHO has a significant influence on the chemical production of CO and the trend in Inv2 (Zheng et al., 2019). Tropospheric columns of OMI HCHO have been reported to keep increasing over China, likely due to significant increases in NMVOC emissions (Li & Wang, 2019; Shen et al., 2019). This could explain why CO emission estimates continue to decrease in Inv2, while Inv1 flattens out since the optimized emissions are overestimated to compensate for the underestimation of CO photochemical production.

In the United States, the CO inversion estimates from Zheng and Jiang are similar to the U.S. NEI regional inventory in terms of trends and have an average positive bias of about 8% (Figure 1). Both estimates follow the continuing decreasing trend of the regional inventory up to 2010, after which Jiang's estimates diverge and indicate a stabilization in CO emissions in the United States. Jiang et al. (2017) attribute this slowdown of U.S. pollutant reduction to factors such as diminished returns on improved catalytic converters which they suggest are unaccounted for in the U.S. inventory (Jiang et al., 2018). Jiang et al. (2018) demonstrate that satellite retrievals and surface measurements also indicate a significant reduction in the decreasing trends of CO and NO_x concentrations after 2010 as compared to the previous years, corroborating the

trend shown in their CO inverse estimates. However, there is not always a direct linear relationship between anthropogenic NO_x emissions and measurements of tropospheric NO_2. This point is further discussed in the following section on NO_x emissions.

In Europe, Zheng's CO inversion estimates match fairly well the general trends from the bottom-up inventories, which show a steady declining trend from the year 2000 that slows down after 2009. Zheng's estimates show a lot of interannual variability, while Jiang's estimates show higher emissions in 2015 than in 2009, indicating a slightly positive recent trend that is contrary to the inventories (Figure 1). In terms of magnitude of emissions, all of the inversion estimates are considerably higher, except for that of Müller which is very similar to the CAMS-REG-AP regional inventory as discussed above. Zheng et al. (2019) suggest that the bottom-up inventories underestimate emissions in these regions and show that their model biases are reduced compared to independent ground-based CO measurement when the posterior emissions are used. However, given that Europe is a region where there is a relatively high level of detailed emission information, the higher inverse estimates of Zheng and Jiang may be due to higher OH levels in their model, since the estimates by Müller (2018), using methylchloroform-constrained OH abundances, provide an excellent agreement with the bottom-up inventories.

The largest uncertainly among the inversion estimates is found in Western Africa, where the CO emissions range from 17 Tg (Jiang-colm) to 64 Tg (Zheng-Inv2) in 2010 (Figure 1). However, Jiang's estimates are likely biased towards the low-end because they are influenced by the low a priori emissions used in their inversion method. The scheme used to partition emissions into separate categories (e.g., anthropogenic and biomass burning) is different in each inversion system (see the supporting information and references therein) and based on information from the a priori emissions. Therefore, this can account for small differences between inversion estimates, particularly in regions such as Western Africa where there is a large contribution from non-anthropogenic sources, such as biomass burning. In addition, the data used to construct bottom-up inventories (e.g., emission factors and activity data) in Africa also have quite large uncertainties. The DACCIWA and DICE-Africa regional inventories both show similar increasing trends in CO emissions. The DACCIWA estimate is about 33% higher than DICE-Africa in 2010; however, there are some sectors not included in DICE-Africa (e.g., on-grid energy and formal industry; see the supporting information for details) which accounts, at least in part, for the discrepancy.

In India, the inversion estimates are largely within the range of the global inventories and the regional inventory REASv3.1; however, they are almost twice as high as Sharma's estimate. The trends are similar to the inventories until about 2012, after which the inverse estimates begin to stabilize (Figure 1). Because India is one of the regions in which updated regional emission data is not easily available, it is difficult to evaluate the trend in CO emissions seen in the estimates. Although not shown here, Sharma projects a value of 53.9 Tg for the year 2021, indicating an increasing trend in CO emissions in India.

4.2. NO_x

Figure 2 displays annually averaged NO_x emissions for each region. Inversion estimates are shown for TCR-2, Qu-NASA, and Qu-DOMINO in all regions and Qu in China and India. Qu-single and Qu-joint are both derived using the same hybrid 4D-Var/mass balance inversion method. The “single” estimates are constrained by only NO_2 observations, and the “joint” estimates are constrained by NO_2 and SO_2, as described in section 2. We recall from section 2 that Qu's joint and single estimates are for India only, while the TCR-2 and inventory emission averages are for India+ (Figure S1) which is a larger region encompassing neighboring countries such as Pakistan, Nepal, and Bangladesh. Qu's estimates would likely be 15–25% higher if they included India+. Although there is a slight difference in the magnitude between the “single” and “joint” species estimates, the results in China and India indicate that this difference is minor compared to the spread in the top-down emission estimates, at least at the regional scale. Qu, Henze, Theys, et al. (2019) report large differences at grid scale, but not in the national budget between the “single” and “joint” inversions. The other two estimates from Qu et al. (2020), Qu-NASA and Qu-DOMINO, allow us to assess to the impact of different satellite products on the top-down NO_x emission estimates (see section 2 for details). An intercomparison of the magnitudes of NO_2 vertical column densities from these two products, as well as from the QA4ECV product used to constrain the TCR-2 emissions, is given in the supporting information of Qu et al. (2020). They reported that the DOMINO NO_2 columns are considerably higher than in the other

products, particularly in eastern China, eastern United States, and parts of Europe. This result is consistent with the top-down emissions presented here: the estimates constrained by the DOMINO retrieval are considerably higher than those constrained by the NASA (Qu-NASA) or QA4ECV (TCR-2) retrievals in all regions. These results emphasize that the uncertainty from satellite retrievals contributes a great deal to the uncertainty in top-down NO_x emissions as noted by other studies (e.g. Kemball-Cook et al., 2015). The percentage of the spread among the top-down inventories ranges from 41% in the United States to 90% in Western Africa, which is considerably higher than the 11% and 60% respective spread found among the bottom-up inventories (Table 3).

The range in emissions among the bottom-up inventories in 2010 for China, Western Africa, India+, and Western Europe (15.6–25.4, 3.5–4.2, 0.7–1.3 and 4.1–6.9 Tg, respectively) exceeds 50% of the ensemble mean (Table 3). The range is lowest in the United States, 7.9–8.8 Tg, which is about 11% of the ensemble mean in 2010. In terms of trends in NO_x emissions, the degree of agreement among the inversion estimates and the inventories varies regionally (Figure 2). In China, the trends are consistent with the regional inventories (MEICv1.3, REASv3.1, and Sun) and the CEDS global inventory, all of which show a broad peak around 2011–2012, followed by a sharp decline. This declining trend is not found in the other global inventories. As mentioned above, the spread among the top-down estimates is larger than the bottom-up estimates. For example, the Qu-single estimate for 2012 is the lowest of the top-down estimates (~17 Tg NO), while the Qu-DOMINO estimate is about 60% higher (~29 Tg NO). Among the bottom-up inventories, CEDS is the highest (~25 Tg NO), which is about 50% higher than the lowest value given by Sun et al. (2018) (~16 Tg NO_x).

In the United States and Europe, the TCR-2 and Qu-NASA inversion estimates of NO_x emissions generally follow the decreasing trends shown in the bottom-up inventories, except in recent years where they show a tendency towards a stabilization of emissions, while the bottom-up inventories indicate a continuing significant decline (Figure 2). In the United States between 2010 and 2016, the TCR-2 and Qu-NASA NO_x emissions decreased by about 1.5% and 0.5%, respectively, per year on average, while the U.S. regional inventory shows a continuously strong reduction of almost 4.5% per year. Jiang et al. (2018) also report a slowdown of the decreasing trend in CO and NO_x top-down emissions in the United States inferred by satellite NO_2 data and suggest that the method used to calculate the NEI U.S. emissions leads to an overestimation of the reduction of emissions after 2010, whereas an alternative fuel-based method could produce trends more consistent with the top-down estimates. Furthermore, the top-down emissions were found to be more consistent with observed ozone concentrations than the U.S. inventory (He et al., 2019). In contrast, Silvern et al. (2019) assert that the continued decreasing trend in the U.S. national inventory is consistent with the trends in NO_2 surface observations and that the stabilization in the OMI NO_2 trend, and the TCR-2 NO_x estimates, could be attributed to an underestimate of free tropospheric NO_2 background in the models. They suggest that increases in the relative contribution of non-anthropogenic background sources of NO_x (e.g., lightning and soils) explain the discrepancy between trends in OMI NO_2 and the NEI inventory. Furthermore, several studies have reported that in rural areas, strong nonlinear relationships exist between anthropogenic NO_x emissions and satellite NO_2 columns, implying that constraining NO_x emissions by NO_2 satellite retrievals might lead to inaccurate estimates (Lamsal et al., 2011; Li & Wang, 2019; Vinken et al., 2014). Laughner and Cohen (2019) reported changes in NO_x lifetime for many U.S. cities and suggested that accounting for this change in lifetime more accurately (for example, by using models with higher resolution) should help to improve emission trend estimates. Clearly, a better understanding is urgently needed of the relationship between NO_x emissions and NO_2 spaceborne columns, as well as of natural emissions and uncertainties in bottom-up NO_x emission estimates.

In general, in India and West Africa the top-down emissions show a weaker increasing trend than the inventories (Figure 2). For example, in Western Africa for the period 2005–2015, the TCR-2 and Qu-NASA estimates increase by about 1.5% yr^{-1}, while the regional inventory DACCIWA increases by more than 3.5% yr^{-1} and DICE-Africa increases by more than 2% yr^{-1} (2006–2013). Similarly, in India during the period 2010–2015, NO_x emissions given by REASv3.1 increase by almost 5% yr^{-1}, while the inversion estimates of TCR-2, Qu-DOMINO, and Qu-NASA increase at slower rates of about 2.5, 2.6, and 1.4% yr^{-1}, respectively. In 2011, the TCR-2 estimates 7.9 Tg NO_x which is in very good agreement with Sharma's value of 7.6 Tg NO_x.

4.3. NMVOCs, SO_2, and Carbonaceous Aerosols

Fewer inventories and inverse estimates are available for these species compared to CO and NOx. Figures 3a and 3b show the annually averaged NMVOC inversion emission estimates in China from Stavrakou and Cao, along with the global and regional inventories. Note that Cao's estimate in Figure 3a represents an average of four inversion experiments, ranging from 16.4 to 23.6 Tg NMVOC, using different combinations of satellite observations as described in Cao et al. (2018). The significant spread, 6.5 Tg, reflects uncertainty in the satellite data and its impact on top-down NMVOC estimates. The inventories lie within a narrow range, although this does not necessarily indicate less uncertainty (Figure 3a). Cao's estimate for 2007 (20.2 Tg NMVOC) is slightly below the range of the bottom-up inventories (21.0–23.6 Tg NMVOC) and is quite close to the REASv3.1 estimate for 2007 (21.0 Tg NMVOC). Stavrakou's estimates are similar in magnitude to the inventories and exhibit a stronger interannual variability. The inventories show an increasing trend in NMVOC emissions in China until ca. 2012, after which they start to level out. Over 2005–2014, Stavrakou's estimates indicate a weak positive trend of approximately 1.4% yr^{-1}, which is lower than those of REASv3.1 (5.2% yr^{-1} over 2005–2014), Li et al. (3.2% yr^{-1}), and MEICv1.3 (3.4% yr^{-1} over 2008–2014). The top-down emission trend is primarily driven by the tropospheric HCHO column trend, amounting to 1.3% yr^{-1} over Northern China between 2005 and 2014 (Stavrakou et al., 2017). Note that the modeling study of Shen et al. (2019) recently reported very similar summertime HCHO trends over Northern China over 2005–2016 (approximately 1% yr^{-1}), and they found a good consistency with corresponding HCHO trends calculated by the GEOS-Chem CTM driven by MEICv1.3 emissions. The reasons for the apparent discrepancy with Stavrakou's results are unclear but might be related to intermodel differences.

Annually averaged SO_2 emissions for China and India are illustrated in Figures 3c and 3d with inversion estimates from Qu and TCR-2 for both regions. The two estimates from Qu are derived using identical methods, except the emissions are constrained using different OMI satellite retrievals (Qu-BIRA and Qu-NASA; Qu, Henze, Li, et al., 2019) The impact of the two different retrievals on the magnitude of emissions is more significant in China where the average difference in annual SO_2 emission estimates is about 20%. In India, this difference is around 6%, a consequence of the fact that differences in the satellite retrievals are not the same in all regions as highlighted in Qu et al. (2020). Both estimates indicate relatively similar trends in China and India between the two OMI SO_2 products. A third estimate of SO_2 emission from Qu (Qu-joint) was derived using satellite SO_2 and NO_2 constraints simultaneously, as described in section 2. This joint method can provide more accurate constraints on emissions due to synergistic changes in O_3 and OH concentrations (Qu, Henze, Theys, et al., 2019). We recall that the Qu-joint inversion estimates are for India only, unlike the other inversion and bottom-up estimates which are for India+. The Qu-joint estimate would be roughly 25% higher if it included India+.

In China, the range of SO_2 emissions is large in both the inversion estimates and the bottom-up inventories (Figures 3c and 3d). For example, in 2010 the inversion estimates range from approximately 17 (TCR-2) to 24 (Qu-BIRA) Tg SO_2, and the inventories range from about 16 (Sun) to 35 (CEDS) Tg SO_2. While the inversion estimates show a significant decrease in Chinese emissions after 2010, this decline is not as steep as in the regional REASv3.1 and MEICv1.3 inventories in which SO_2 emissions decreased by about 35% and 40% between 2011 and 2015, respectively. In general, the inversion estimates are significantly lower than in the regional inventories until after 2014.

In India, SO_2 emissions derived from the inversion systems are all considerably lower than what is reported in most inventories which ranges from 10.7 to 13.9 Tg in 2010 (Figure 3d). The exception is Sharma's bottom-up estimate for 2011 of 6.5 Tg SO_2 which is considerably lower than the other inventories and closer to the inversion estimates. Even if we add 25% to Sharma's estimates for India to account for the other countries included in the India+ region, it is still the less than the other bottom-up estimates. The top-down estimates range from 4.1 to 6.2 Tg in 2010. The inventories all indicate that emissions have been steadily increasing in India since about 2005; however, this trend is weaker in the inversion estimates. The weaker trends in the inversion estimates could be partly due to the lack of vertical sensitivity of the satellite sensors in the UV-spectral range where SO_2 is being retrieved. Posterior SO_2 emissions in less polluted areas are harder to estimate due to the large amount of negative retrievals (Qu, Henze, Theys, et al., 2019). For these reasons, most inverse modeling studies have focused on regions where SO_2 concentrations have been high in recent years such as Asia.

Figure 4 shows annually averaged black and organic carbon emissions in China, India, and Western Africa. Chen's inverse emission estimates provide a unique global time series for the period 2006–2011, as a first attempt in using an inversion approach to indirectly derive black and organic carbon emissions by fitting satellite measurements of spectral aerosol extinction (AOD) and absorption (AAOD) (Chen et al., 2019). The inversion estimates of BC emissions are within the range of the bottom-up inventories in China and Western Africa and slightly below in India (Figure 4). In contrast, the inversion estimates of anthropogenic OC emissions are considerably higher than most inventories in China and Western Africa and at the upper end of the range in India. It is interesting to note that Chen's estimates and the DACCIWA regional inventory show considerably higher OC emissions than the global inventories and the regional inventory DICE-Africa, while BC emissions are quite similar. This could suggest an underestimation in OC emissions in the global inventories in these regions. Other studies have identified inaccuracies in global inventories in West Africa where there is much uncertainty related to the emission factors and activity data from region-specific emissions sources which are unaccounted for (Liousse et al., 2014; Marais & Wiedinmyer, 2016). For example, wood burning for cooking and heating is a large source of OC and BC emissions in Africa but is likely misrepresented in inventories due to lack of representative data. Inversion estimates could potentially be used to improve inventory emissions from these and other misrepresented sources. However, uncertainties in the inversion estimation of black and organic carbon by fitting indirectly measurements of AOD/AAOD need to also be better quantified. Both the BC and OC inversion estimates show a stronger interannual variability than the bottom-up inventories, but in most cases the general trends agree reasonably well.

5. Comparison of Recent Emission Trends With SSPs for Different Regions

In this section, we compare recent trends from available inventories and inversion estimates to the five SSP scenarios under consideration. Linear trends of NO_x and CO emissions from the SSPs for the years 2010–2020 and the ensemble mean trend (EMT) from the bottom-up and top-down inventories which have data until at least 2015 are summarized in Table 4. All trends are expressed in % yr^{-1} relative to the mean over the data period. Individual trends and their statistical significance are given in the supporting information. Note that for the CO EMT, we include only the Zheng et al. (2019) estimates from the inversion using the most recent satellites constraints for CO, HCHO, and CH_4 (inversion 3, cf. section 2) and the Jiang-prof estimates which assimilate profile data. For each region, the SSP trends which differ by less than 1% compared to the EMT trend are in bold, indicating the scenarios with recent trends that are closest to those of the inventories and inverse modeling emissions. This type of analysis is to a certain extent speculative; therefore, the results only indicate suggestions of the scenarios which match most closely the estimations of actual recent trends. Furthermore, recent trends in the last 10 years are not necessarily indicative of how emissions will evolve in the future. Recall that SSP1 and SSP5 are both strong pollution control scenarios; SSP5 assumes an energy-intensive, fossil fuel-based economy, while SSP1 represents a future shifted towards more sustainable practices. SSP3 and SSP4 represent futures with more pessimistic development trends, where there is little investment in health and education and fast growing populations. In SSP3, national and regional security is prioritized, whereas in SSP4 large inequalities dominate both within and across countries. SSP2 is the moderate pollution control scenario, in which trends more or less follow their historical patterns.

In China, SSP126 is the scenario which matches most closely to the actual recent trends in CO emissions. This is a strong pollution control scenario that reflects the stringent air quality standards China has enforced in recent years. All of the SSP NO_x trends agree with the declining emissions reported by the inventories (REASv3.1, Sun, MEICv1.3) and inverse modeling estimates (Qu-joint, TCR-2), but for the period considered, 2010–2020, the decrease is not as strong. Considering only the last few years since 2015, we can see in Figure 3 that the MEICv1.3 regional inventory shows a declining trend in NO_x emissions in China which is qualitatively similar to that of SSP126. Contrarily, the TCR-2 inversion estimates indicate that CO emissions stabilize after 2016.

The results indicate that recent emission trends in the United States are also similar to SSP126 (Table 4). The EMT, which is based on the NEI regional inventory and inverse modeling estimates, shows recent declines in NO_x and CO emissions on the order of 3% yr^{-1}, consistent with the strong pollution control scenario. However, it should also be noted that the CO inversion estimates from Jiang et al. (2017) which show a

Table 4
Linear Trends of NO_x and CO Emissions From SSPs for the Years 2010–2020 and the Ensemble Mean Trend (EMT) From All Regional Inventories and Inversion Estimates Which Have Data Until at Least 2015 and Are Statistically Significant ($p > 0.05$)

		EMT	SSP126	SSP245	SSP370	SSP460	SSP585	Closest scenario
China	NO_x	−3.07 (*4*)	−1.59	−1.06	0.86	−0.64	−1.03	SSP126
	CO	−2.94 (*3*)	**−2.36**	−1.03	0.36	−0.98	**−2.19**	
Middle East	NO_x	*	0.02	0.44	1.29	−1.39	1.01	—
	CO	*	−2.12	−3.31	−0.12	−1.86	0.02	
Western Africa	NO_x	+2.03 (*2*)	0.59	1.40	**1.92**	**2.08**	2.18	SSP460
	CO	+3.35 (*2*)	−3.52	0.97	1.27	1.30	−0.41	
India	NO_x	+3.33 (*2*)	1.39	2.13	**3.17**	**3.05**	4.35	SSP370
	CO	+1.32 (*3*)	−2.03	**0.95**	**1.81**	2.10	0.23	
United States	NO_x	−3.16 (*2*)	−3.98	−4.80	−2.47	**−3.19**	**−2.99**	SSP126
	CO	−3.70 (*3*)	**−3.54**	−2.02	−1.28	−2.34	−1.21	
Western Europe	NO_x	−2.20 (*2*)	−4.86	−4.86	−3.44	−4.12	**−3.12**	SSP126
	CO	−4.21 (*1*)	**−3.87**	**−4.19**	−1.48	−2.50	−2.80	
Central Europe	NO_x	−3.44 (*1*)	**−4.21**	**−4.34**	−2.46	−3.11	−2.46	SSP126
	CO	−3.20 (*1*)	−3.72	−1.01	−0.93	−0.03	**−3.18**	
South America	NO_x	*	−0.07	−0.41	1.12	−0.52	0.94	—
	CO	*	−2.56	−2.85	−0.47	−1.31	−1.74	
Southeast Asia	NO_x	+2.07 (*2*)	**1.84**	0.45	2.07	2.00	**1.35**	SSP126
	CO	−2.72 (*2*)	**−3.02**	−0.97	1.05	0.84	−0.08	
Indonesia	NO_x	+1.43 (*2*)	0.61	0.08	2.01	**1.44**	**1.41**	SSP460
	CO	+2.86 (*2*)	−3.15	−1.83	0.50	0.65	−0.63	
Oceania	NO_x	*	−0.75	−0.38	0.36	−0.32	0.17	—
	CO	−5.90 (*1*)	−3.17	−1.07	−1.21	−2.08	−0.91	
Southern Africa	NO_x	+2.91 (*1*)	−0.19	0.21	0.76	0.32	0.32	—
	CO	+3.04 (*2*)	−2.53	0.80	1.11	1.28	−0.37	

Note. Trends are expressed in units of % yr^{-1} relative to the mean over the data period. The number of available datasets with statistically significant trends used to calculate the average is indicated in parenthesis. SSP trends shown in bold correspond most closely to recent observed trends for NO_x and CO.

slowdown in declining CO emissions in the United States are not included in the EMT because there is not a statistically significant trend. If the Jiang et al.'s (2017) inversion estimates are included, the EMT would show less of a negative trend in CO emissions more similar to that of SSP585. In Western and Central Europe, as in the United States, there is a smaller spread in emissions among the SSPs, especially during the early century; therefore, the trends are more similar and indicate the same sign. Trends from SSP126 and SSP585 match most closely to the EMT for Europe, both of which are strong pollution control scenarios. However, it should be noted that the inversion estimates of CO (Jiang et al., 2017, and Zheng et al., 2019) do not show a statistically significant trend in recent years in Europe and therefore are not included in the EMT which is based largely on the CAMS-REG-AP regional inventory (Figures 1 and 2). In Southeast Asia, the strong pollution control scenario SSP126 also matches the EMT most closely, which indicates a positive trend in NO_x and declining trend in CO emissions.

Our results, based on the trends given in Table 4 as well as a qualitative visual interpretation of Figures 1 and 2, indicate that the most likely scenario representing recent emission trends in India is SSP370 which is a low pollution control scenario. In Western Africa and Indonesia+, emission trends from SSP460 match most closely to the recent EMT in NO_x and CO emissions. SSP4, also a low pollution control scenario, represents a scenario with a fast-growing population with increasing inequalities, leading to societies that are highly vulnerable to climate change. Indeed, air quality is deteriorating in many West African countries due to rapid increases in population, economic growth, and coinciding lack of regulations, especially in megacities (Liousse et al., 2014). For some of the regions the results are ambiguous, either because none of the SSP emission trends are close to the actual trends (i.e., Southern Africa), or because there is not a statistically significant EMT (i.e., Middle East and South America). In general, and especially in regions where there is a lack of reliable emission data, the results should be interpreted with caution in terms of robustness.

6. Discussion and Conclusions

In this study, we have presented a comprehensive overview and comparison of current state-of-the-art top-down and bottom-up emission estimates of CO, NO_x, NMVOC, SO_2, BC, and OC for several world regions. The results show that while the top-down estimates are within the range of bottom-up emission inventories for some regions, they often exhibit a larger range of uncertainty. In general, for all species the largest discrepancies are found outside of regions such as the United States, Europe, and Japan where the most accurate and detailed information on emissions (e.g., activity data, emission factors) is available. In terms of absolute magnitude, the largest spread in CO and NO_x is found in China where in 2010 differences are approximately 90 (~60%) and 10 (~50%) Tg, respectively, among the bottom-up inventories and 25 (~8%) and 12 (~60%) Tg, respectively, among the top-down inventories (Table 3). Significant differences among the bottom-up inventories are also seen for other compounds in China: ~20 Tg (~80%) for SO_2, 2 Tg (~55%) for OC, and ~1 Tg (~60%) for BC. Contrarily, NMVOC inventory emissions are in better agreement in China, with a difference of ~4 Tg (~15%) in 2010, as compared to most other regions (e.g., ~8 Tg [~90%] in Western Africa and ~8 Tg [~45%] in India+). This agreement might be coincidental, however, and does not necessary imply that the emissions are less uncertain. A large spread also exists among the inventories for Western Africa. The percentage of the range among the inventories relative to the ensemble mean for CO and NO_x emissions is 45% and 60%, respectively, for the bottom-up inventories and 119 and 90%, respectively, for the top-down inventories (Table 3). In India the spread is also large, but higher for NO_x emissions among the bottom-up (59%) and top-down (69%) inventories than for CO emissions (24 and 20%, respectively).

Top-down emission estimates offer great potential and clear advantages; however, future work aimed at identifying, quantifying, and reducing the uncertainties is needed. Constraining multiple species in inversion modeling methods can lead to better consistency in simulated atmospheric chemical processes and thus more accurate optimized emissions (e.g., Qu, Henze, Theys, et al., 2019; Zheng et al., 2019). Correctly modeling OH fields are also important due to its significant impact on oxidation processes (Müller, 2018; Jiang, 2011; Miyazaki 2020). More generally, the representation of chemical and transport processes in model should be improved. In addition, the type of satellite data assimilated (e.g., profile vs. total column) has a large impact on inversions (e.g., Jiang et al., 2017) and should be further explored. Finally, the satellite retrievals have important uncertainties with significant impacts on the emission inversions. Much can be learned in terms of quantifying these and other sources of uncertainty in inverse modeling estimates through more collaborated intercomparison projects such as the Global Carbon Project (www.globalcarbonproject.org) which targets CO_2 and CH_4. A first step has been made with the IGAC AMIGO project (Analysis of eMIssions usinG Observations, https://amigo.aeronomie.be/) which brings together the international scientific community with the common goal of better quantifying emissions for a variety of trace gases and at different spatio-temporal scales. Inverse modeling has been identified as an integral part of AMIGO.

Top-down emissions offer great potential to supplement or improve bottom-up inventories, particularly in regions where global inventories often lack the necessary up-to-date and accurate information regarding regional activity data and emission factors. For example, China has undergone rapid economic growth in addition to stringent pollution control policies in recent years, both of which have led to rapidly changing activity data and emission factors (Zheng, Tong, Liu et al., 2018). This evolution has had a large impact on emissions, which were estimated to have been decreasing substantially in China during the last several years, except for NMVOC. The downward trend in China's emissions is well captured by the inversion estimates, as well as (Rao et al., 2017) by the detailed regional inventories, but is not represented in any of the global inventories. This is a clear example of where inversion estimates provide useful constraints to the global bottom-up inventories, particularly in countries that are undergoing rapid changes in economy, technology, and environmental policies, such as India and Africa. Finally, since inversion estimates become available more quickly than bottom-up inventories, they can be used to extrapolate bottom-up inventories to the most recent years, which would benefit air quality forecasting. This also adds information that can be used to tune baseline emissions in recent years in the development of future emission scenarios such as the RCPs and SSPs.

This study has also compared recent emission trends in regional inventories and inversion estimates to those of five SSP near-future projections for several world regions. For each region, we identified the scenarios for

which the ensemble mean CO and NOx trends for the recent years (2010–2020) match most closely the best estimates based on bottom-up and top-down estimates. This type of analysis can be helpful in updating inventories for the most recent years and can serve as a guide in selecting CMIP6 climate change projections to be used for regional downscaling in air quality forecasting and near-future pollution control/mitigation and climate impact studies. In addition, highlighting inconsistencies between the SSPs and actual emissions can help improve in the development of future emission scenarios. Not surprisingly for China, which has experienced drastic reductions in emissions due to the enforcement of stringent air quality policies, the trends from the strong pollution control scenarios, SSP1 and SPP5, are most representative of the actual recent trend. In India and Western Africa, regions of rapid population growth and significant increases in unregulated emissions, SSP3 and SSP4 which represent futures with more pessimistic development trends (e.g., little investment in health and education and fast growing populations) match most closely the actual recent trends.

Acknowledgments

We would like to thank the two anonymous reviewers for their contributions in improving the final version of this manuscript. This study has received support from the CAMS (Copernicus Atmospheric Monitoring System) project and contributes to the AMIGO (Analysis of eMIssions usinG Observations, https://amigo.aeronomie.be/) project of the International Global Atmospheric Chemistry (IGAC) project. This research (M. B.) has also been supported by the projects PRODEX TROVA (2016-2018) and TROVA-E2 (2019) of the European Space Agency (ESA) funded by the Belgian Science Policy Office, as well as by the SOLFEO project funded by ESA. We acknowledge the use of data products from the NASA AURA and EOS Terra satellite missions. We also acknowledge the free use of tropospheric NO_2 column data from the SCIAMACHY, GOME-2, and OMI sensors from www.temis.nl. Part of this work was conducted at the Jet Propulsion Laboratory, California Institute of Technology, under contract with the National Aeronautics and Space Administration (NASA). D. K. H. and Z. Q. recognize support from NASA ACMAP and HAQAST.

References

Anderson, D. C., Loughner, C. P., Diskin, G., Weinheimer, A., Canty, T. P., Salawitch, R. J., et al. (2014). Measured and modeled CO and NO y in DISCOVER-AQ: An evaluation of emissions and chemistry over the eastern US. *Atmospheric Environment*, *96*, 78–87. https://doi.org/10.1016/j.atmosenv.2014.07.004

Arellano, A. F., Kasibhatla, P. S., Giglio, L., Van der Werf, G. R., & Randerson, J. T. (2004). Top-down estimates of global CO sources using MOPITT measurements. *Geophysical Research Letters*, *31*, 1929. https://doi.org/10.1029/2002GL015609

Boersma, K. F., Eskes, H. J., Dirksen, R. J., vander, A. R. J., Veefkind, J. P., Stammes, P., & Brunner, D. (2011). An improved tropospheric NO_2 column retrieval algorithm for the Ozone Monitoring Instrument. *Atmospheric Measurement Techniques*, *1905–1928*. https://doi.org/10.5194/amt-4-1905-2011

Bouwman, A., Kram, T., & Goldewijk, K. (2006). *Integrated modeling of global environmental change. An overview of IMAGE 2.4*, Bilthoven: Netherlands Environmental Assessment Agency (MNP) publications.

Cao, H., Fu, T.-M., Zhang, L., Henze, D., Miller, C., Lerot, C., & Zhao, Y. (2018). Adjoint inversion of Chinese non-methane volatile organic compound emissions using space-based observations of formaldehyde and glyoxal. *Atmospheric Chemistry and Physics*, *18*, 15,017–15,046. https://doi.org/10.5194/acp-18-15017-2018

Chen, C., Dubovik, O., Henze, D. K., Chin, M., Lapyonok, T., Schuster, G. L., & Torres, B. (2019). Constraining global aerosol emissions using POLDAR/PARASOL satellite remote sensing observations. *Atmospheric Chemistry and Physics*, *19*, 14,585–14,606. https://doi.org/10.5194/acp-19-14585-2019

Chen, C., Dubovik, O., Henze, D. K., Lapyonak, T., Chin, M., Ducos, F., & Li, L. (2018). Retrieval of desert dust and carbonaceous aerosol emissions over Africa from POLDER/PARASOL products generated by the GRASP algorithm. *Atmospheric Chemistry and Physics*, *18*, 12,551–12,580. https://doi.org/10.5194/acp-18-12551-2018

Crippa, M., Guizzardi, D., Muntean, M., Schaaf, E., Dentener, F., Aardenne, J. A., et al. (2018). Gridded emissions of air pollutants for the period 1970–2012 with EDGARv4.3.2. *Earth System Science Data*, *10*, 1987–2013. https://doi.org/10.5194/essd-10-1987-2018

Dubovik, O., Herman, M., Holdak, A., Lapyonok, T., Tanré, D., Deuzé, J. L., & Lopatin, A. (2011). Statically optimized inversion algorithm for enhanced retrieval of aerosol properties from spectral and mutli-angle polarimetric satellite observations. *Atmospheric Measurement Techniques*, *4*. https://doi.org/10.5194/amt-4-975-2011

Dubovik, O., Lapyonok, T., Litvinov, P., Herman, M., Fuertes, D., Ducos, F., et al. (2014). GRASP: a versatile algorithm for characterizing the atmosphere. *SPIE Newsroom*. https://doi.org/10.1117/2.1201408.005558

Elguindi, N., Darras, S., Granier, C., & Guevara, M. (2020). CAMS global anthropogenic emissions. https://doi.org/10.24380/fw9g-2t24

Eyring, V., Bony, S., Meehl, G., Senior, C., Stevens, B., Stouffer, R., & Taylor, K. (2016). Overview of the Coupled Model Intercomparison Project Phase 6 (CMIP6) experimental design and organization. *Geoscientific Model Development*, *9*. https://doi.org/10.5194/gmd-9-1937-1026

George, M., Clerbaux, C., Bouarar, I., Coheur, P.-F., Deeter, M., Edwards, D., et al. (2015). An examination of the long-term CO records from MOPITT and IASI: Comparison of retrieval methodology. *Atmospheric Measurement Techniques*, *8*, 4313–4328. https://doi.org/10.5194/amt-8-4313-2015

Gidden, M. J., Riahi, K., Smith, S. J., Fujimori, S., Luderer, G., Kriegler, E., et al. (2019). Global emissions pathways under different socioeconomic scenariosfor use in CMIP6: A dataset of harmonized emissions trajectoriesthrough the end of the century. *Geoscientific Model Development*, *12*, 1443–1475. https://doi.org/10.5194/gmd-12-1443-2019

Granier, C., Bessagnet, B., Bond, T., D'Angiola, A., Denier van der Gon, H., Frost, G. J., et al. (2011). Evolution of anthropogenic and biomass burning emissions of air pollutants at global and regional scales during the 1980–2010 period. *Climatic Change*, *109*(1-2), 163–190. https://doi.org/10.1007/s10584-011-0154-1

Granier, C., Darras, S., Denier van der Gon, H., Doubalova, J., Elguindi, N., Galle, B., et al. (2019). *The Copernicus Atmosphere Monitoring Service global and regional emissions*, Reading, United Kingdom: Copernicus Atmosphere Monitoring Service. https://doi.org/10.24380/d0bn-kx16

He, T.-L., Jones, D. B., Huang, B., Liu, Y., Miyazaki, K., Jiang, Z., & Worden, J. R. (2019). *Recurrent U-net: Deep learning to predict daily summertime ozone in the United States*. arXiv:1908.05841 Ithaca, New York: Cornell University.

Henze, D. K. (2009). Inverse modeling and mapping US air quality influences of inorganic PM2.5 precursor emissions using the adjoint of GEOS-Chem. *Atmospheric Chemistry and Physics*, *9*, 5877–5903. https://doi.org/10.5194/acp-9-5877-2009

Henze, D. K., Hakami, A., & Seinfeld, J. H. (2007). Development of the adjoint of GEOS-Chem. *Atmospheric Chemistry and Physics*, *7*. https://doi.org/10.5194/acp-7-2413-2007

Hosley, R., Smith, S., Feng, L., Klimont, Z., Janssens-Maenhout, G., & Pitkanen, T. (2018). Historical (1750–2014) anthropogenic emissions of reactive gases and aerosols from the Community Emissions Data System (CEDS). *Geoscientific Model Development*, *11*. https://doi.org/10.5194/gmd-11-369-2018

Hudman, R. C., Murray, L. T., Jacob, D. J., Millet, D. B., Turquety, S., Wu, S., et al. (2008). Biogenic versus anthropogenic sources of CO in the United States. *Geophysical Research Letters*, *35*, L04801. https://doi.org/10.1029/2007GL032393

Janssens-Maenhout, G., Crippa, M., Guizzardi, D., Dentener, F., Muntean, M., Pouliot, G., et al. (2015). HTAP_v2.2: a mosaic of regional and global emission grid maps for 2008 and 2010 to study hemispheric transport of air pollution. *Atmospheric Chemistry and Physics*, *15*, 11,411–11,432. https://doi.org/10.5194/acp-15-11411-2015

Jiang, Z., McDonald, B. C., Worden, H., Worden, J. R., Miyazaki, K., Qu, Z., et al. (2018). Unexpected slowdown of US pollutant emission reduction in the past decade. *Proceedings of the National Academy of Sciences*, *115*(20), 5099–5104. http://doi.org/10.1073/pnas.1801191115

Jiang, Z., Jones, D., Worden, H., Deeter, M., Henze, D., Worden, J., & Schuck, T. (2013). Impact of model errors in convective transport on CO source estimates inferred from MOPITT CO retrievals. *Journal of Geophysical Research: Atmospheres*, *118*, 2073–2083. https://doi.org/10.1002/jgrd.50216

Jiang, Z., Jones, D., Worden, J., Worden, H., Henze, D., & Wang, Y. (2015). Regional data assimilation of multi-spectral MOPITT observations of CO over North America. *Atmospheric Chemistry and Physics*, *15*, 6801–6814. https://doi.org/10.5194/acp-15-6801-2015

Jiang, Z., Worden, J., Worden, H., Deeter, M., Jones, D., Arellano, A., & Henze, D. (2017). A 15-year record of CO emissions constrained by MOPITT CO observations. *Atmospheric Chemistry and Physics*, *17*, 4565–4583. https://doi.org/10.5194/acp-17-4565-2017

Jiang, Z. D. (2011). Quantifying the impact of modelerrors on top-down estimates of carbon monoxide emissions using satellite observations. *Journal of Geophysical Research*, *116*, D15306. https://doi.org/10.1029/2010JD015282

Keita, S., Liousse, C., Doumbia, T., Touré, E. N., Sylvain, G., Elguindi, N., et al. (2020). African Anthropogenic Emissions Inventory for gases and particles from 1990 to 2015 (DACCIWA). https://doi.org/10.25326/56

Kemball-Cook, S., Yarwood, G., Johnson, J., Dornblaser, B., & Estes, M. (2015). Evaluating NO_x emission inventories for regulatory air quality modeling using satellite and air quality model data. *Atmospheric Environment*, 1–8. https://doi.org/10.1016/j.atmosenv.2015.07.002

Kriegler, E., Edmonds, J., Hallegatte, S., Ebi, K. L., Kram, T., Riahi, K., et al. (2014). A new scenario framework for climate change research: the concept of shared climate policy assumptions. *Climatic Change*, *122*, 401–414. https://doi.org/10.1007/s10584-013-0971-5

Krotkov, N. A., Lamsal, L. N., Celarier, E., Swartz, W., Marchenko, S., Bucsela, E. J., et al. (2017). The version 3 OMI NO2 standard product. *Atmospheric Measurement Techniques*, *10*. https://doi.org/10.5194/amt-10-3133-2017

Kuenen, J., Visschedijk, A. J., Jozwicka, M., & Denier van der Gon, H. (2014). TNO-MACC_II emission inventory: A multi-year (2003–2009) consistent high-resolution European emission inventory for air quality modeling. *Atmospheric Chemistry and Physics*, *14*, 10,963–10,976. https://doi.org/10.5194/acp-14-10963-2014

Kurokawa, J., & Ohara, T. (2019). Long-term historical trends in air pollutant emissions in Asia: Regional Emission inventory in ASia (REAS) version 3.1. *Atmospheric Chemistry and Physics Discussions*. https://doi.org/10.5194/acp-2019-1122

Lamsal, L., Martin, R., Padmanabhan, A., Donkelaar, A. v., Zhang, Q., Sioris, C., & Newchurch, M. (2011). Application of satellite observations for timely updates to global anthropogenic NO_x emission inventories. *Geophysical Research Letters*, *38*, L05810. https://doi.org/10.1029/2010GL046476

Laughner, J., & Cohen, R. (2019). Direct observation of changing NO_x lifetime in North American cities. *Science*, *366*, 723–727. https://doi.org/10.1126/science.aax6832

Li, C., Joiner, J., Krotkov, N. A., & Bhartia, P. (2013). A fast and sensitive new satellite SO2 retrieval algorithm based on principal component analysis: Application to the Ozone Monitoring Instrument. *Geophysical Research Letters*, *40*, 6314–6318. https://doi.org/10.1002/2013GL058134

Li, J., & Wang, Y. (2019). Inferring the anthropogenic NOx emission trend over the United States during 2003–2017 from satellite observations: Was there a flattening of the emission trend after the Great Recession? *Atmospheric Chemistry and Physics Discussions*, *19*. https://doi.org/10.5194/acp-2019-472

Liousse, C., Assamoi, E., Criqui, P., Granier, C., & Rosset, R. (2014). Explosive Growth in African combustion emissions from 2005 to 2030. *Environmental Research Letters*, *9*. https://doi.org/10.1088/1748-9326/9/3/035003

Lorente, A., Boersma, K., Yu, H., Dörner, S., Hilboll, A., Richter, A., et al. (2017). Structural uncertainty in air mass factor calculation for NO_2 and HCHO satellite retrievals. *Atmospheric Measurement Techniques*, *10*, 759–782. https://doi.org/10.5194/amt-10-759-2017

Marais, E., & Wiedinmyer, C. (2016). Air Quality Impact of Diffuse and Inefficient Combustion Emissions in Africa (DICE-Africa). *Environmental Science and Technology*, *50*. https://doi.org/10.1021/acs.est.6b02602

Miyazaki, K., Bowman, K., Sekiya, T., Eskes, H., Boersma, F., Worden, H., & Ogochi, K. (2020). An updated tropospheric chemistry reanalysis and emission estimates, TCR-2, for 2005–2018. *Earth System Science Data Discussions*. https://doi.org/10.5194/essd-2020-30

Miyazaki, K., Eskes, H., Sudo, K., Boersma, K. F., Bowman, K., & Kanaya, Y. (2017). Decadal changes in global surface NO_x emissions from multi-constituent satellite data assimilation. *Atmospheric Chemistry and Physics*, *17*. https://doi.org/10.5194/acp-17-807-2017

Miyazaki, K., Eskes, H., Sudo, K., Boersma, K. F., Bowman, K., & Kanaya, Y. (2019). Balance of emission and dynamical controls on ozone during the Korea-United States Air Quality campaign from multiconstituent satellite data assimilation. *Journal of Geophysical Research: Atmospheres*, *124*, 387–413. https://doi.org/10.1029/2018JD028912

Miyazaki, K. B. (2020). Evaluation of a multi-model, multi-constituent assimilation framework for tropospheric chemical reanalysis. *Atmospheric Chemistry and Physics*, *20*, 931–967. https://doi.org/10.5194/acp-20-931-2020

Moss, R. H., Edmonds, J. A., Hibbard, K. A., Manning, M. R., Rose, S. K., van Vuuren, D. P., et al. (2010). The next generation of scenarios for climate change research and assessment. *Nature*, *463*(7282), 747–756. https://doi.org/10.1038/nature08823

Müller, J.-F., & Stavrakou, T. (2005). Inversion of CO and NO_x emissions using the adjoint of the IMAGES model. *Atmospheric Chemistry and Physics*, *5*. https://doi.org/10.5194/acp-5-1157-2005

Müller, J.-F. T.-F. (2018). Top-down CO emissions based on IASI observations and hemispheric constraints on OH levels. *Geophysical Research Letters*, *45*, 1621–1629. https://doi.org/10.1002/2017GL076697

O'Neill, B., Tebaldi, C., Vuuren, D. v., Eyring, V., Friedlingstein, P., Hurtt, G., & Sanderson, B. M. (2016). The Scenario Model Intercomparison Project (ScenarioMip) for CMIP6. *Geoscientific Model Development*, *9*. https://doi.org/10.5194/gmd-9-3461-2016

O'Neill, B. C., Kriegler, E., Riahi, K., Ebi, K. L., Hallegatte, S., Carter, T. R., et al. (2014). A new scenario framework for climate change research: the concept of shared socioeconomic pathways. *Climatic Change*, *122*(3), 387–400. https://doi.org/10.1007/s10584-013-0905-2

Qu, Z., Henze, D., Cooper, O., & Neu, J. (2020). Improving NO_2 and ozone simulations through global NO_x emission inversions. *Atmospheric Chemistry and Physics Discussions*. https://doi.org/10.5194/acp-2020-307

Qu, Z., Henze, D. K., Capps, S. L., Wang, Y., Xu, X., Wang, J., & Keller, M. (2017). Monthly top-down NO_x emissions for China (2005–2012): A hybrid inversion method and trend analysis. *Journal of Geophysical Research: Atmospheres*, *122*, 4600–4625. https://doi.org/10.1002/2016JD025852

Qu, Z., Henze, D. K., Theys, N., Wang, J., & Wang, W. (2019). Hybrid mass balance/4D-Var joint inversion of NO_x and SO_2 emissions in East Asia. *Journal of Geophysical Research: Atmospheres*, *124*, 8203–8224. https://doi.org/10.1029/2018JD030240

Qu, Z., Henze, D. K., Li, C., Theys, N., Wang, Y., Wang, J., & Ren, X. (2019). SO_2 emission estimates using OMI SO_2 retrievals for 2005–2017. *Journal of Geophysical Research: Atmospheres*, *124*, 8336–8359. https://doi.org/10.1029/2019JD030243

Rao, S., Klimont, Z., Smith, S. J., Van Dingenen, R., Dentener, F., Bouwman, L., et al. (2017). Future air pollution in the Shared Socio-economic Pathways. *Global Environmental Change*, *42*, 346–358. https://doi.org/10.1016/j.gloenvcha.2016.05.012

Riahi, K., Vureen, D. v., & Kriegler, E. (2017). The Shared Socioeconomic Pathways and their energy, landuse, and greenhouse gas emissions implications: An overview. *Global Environmental Change*, *42*, 153–168. https://doi.org/10.1016/j.gloenvcha.2015.01.004

Sharma, S., & Kumar, A. (2016). *Air pollutant emissions scenario for India*. New Delhi: The Energy and Resources Institute.

Shen, L., Jacob, D. J., Zhu, L., Zhang, Q., Zheng, B., Sulprizio, M. P., & Liao, H. (2019). The 2005–2016 trends of formaldehyde columns over China observed by satellites: Increasing anthropogenic emissions of volatile organic compounds and decreasing agricultural fire emissions. *Geophysical Research Letters*, *46*, 4468–4475. https://doi.org/10.1029/2019GL082172

Silvern, R. F., Jacob, D. J., Mickley, L. J., Sulprizio, M. P., Travis, K. R., Marais, E. A., et al. (2019). Using satellite observations of tropospheric NO2 columns to infer long-term trends in US NOx emissions: the importance of accounting for the free tropospheric NO2 background. *Atmospheric Chemistry and Physics*, *19*(13), 8863–8878. https://doi.org/10.5194/acp-19-8863-2019

Stavrakou, T., Müller, J.-F., Bauwens, M., De Smedt, I., Bouarar, I., Wang, X., & Brasseur, G. (2017). Sources and long-term trends of ozone precursors to Asian Pollution. *Air Pollution in Eastern Asia : an integrated perspective* (167–189). Springer international Publishing.

Stavrakou, T., Müller, J.-F., Boersma, K. F., Vander, A. R. J., Kurokawa, J., Ohara, T., & Zhang, Q. (2013). Key chemical NO_x sink uncertainties and how they influence top-down emissions of nitrogen oxides. *Atmospheric Chemistry and Physics*, *13*, 9057–9082. https://doi.org/10.5194/acp-13-9057-2013

Stavrakou, T., Müller, J.-F., De Smedt, I., Van Roozendael, M., van der Werf, G. R., Giglio, L., & Guenther, A. (2009). Evaluating the performance of pyrogenic and biogenic emission inventories against one decade of space-based formaldehyde columns. *Atmospheric Chemistry and Physics*, *9*. https://doi.org/10.5194/acp-9-1037-2009

Stavrakou, T., Müller, J.-F., Peeters, J., Razavi, A., Clarisse, L., Clerbaux, C., & Paton-Walsh, C. (2012). Satellite evidence for a large source of formic acid from boreal and tropical forests. *Nature Geoscience*, *5*. https://doi.org/10.1038/ngeo1354

Streets, D. G., Canty, T., Carmichael, G. R., Foy, B. d., Dickerson, R. R., Duncan, B. N., & Lu, Z. (2013). Emissions estimation from satellite retrievals: A review of current capability. *Atmospheric Environment*, *77*, 1011–1042. https://doi.org/10.1016/j.atmosenv.2013.05.051

Sun, W., Shao, M., Granier, C., Liu, Y., Ye, C., & Zheng, J. (2018). Long-term trends of Anthropogenic SO_2, NO_x, CO, and NMVOCs emissions in China. *Earth's Future*, *6*, 1112–1133. https://doi.org/10.1029/2018EF000822

Theys, N., Smedt, I. D., Gent, J. V., Danckaert, T., Wang, T., Hendrick, F., et al. (2015). Sulfur dioxide vertical column DOAS retrievals from the Ozone Monitoring Instrument: Global observations and comparison to ground-based and satellite data. *Journal of Geophysical Research: Atmospheres*, *120*, 2470–2491. https://doi.org/10.1002/2014JD022657

van Vuuren, D., Edmonds, J., Kainuma, M., Riahi, K., Thomson, A., Hibbard, K., et al. (2011). The representative concentration pathways: An overview. *Climate Change*, *109*. https://doi.org/10.1007/s10584-011-0148-z

van Vuuren, D. P., Kreigler, E., O'Neill, B. C., Ebi, K. L., Riahi, K., Carter, T. R., et al. (2014). A new scenario framework for Climate Change Research: Scenario matrix architecture. *Climatic Change*, *122*, 373–386

Vinken, G., Boersma, K. F., Maasakkers, J. D., Adon, M., & Martin, R. (2014). Worldwide biogenic soil NO_x emissions inferred from OMI NO_2 observations. *Atmospheric Chemistry and Physics*, *14*, 10,363–10,381. https://doi.org/10.5194/acp-14-10363-2014

Watanabe, S., Hajima, T., Sudo, K., Nagashima, T., Takemura, T., Okajima, H., & Kawamiya, M. (2011). MIROC-ESM 2010: Model description and basic results of CMIP5-20c3m experiments. *Geoscientific Model Development*, *4*, 845–872. https://doi.org/10.5194/gmd-4-845-2011

Zheng, B., Chevallier, F., Ciais, P., Yin, Y., Deeter, M., Worden, H., & He, K. B. (2018). Rapid decline in carbon monoxide emissions and export from East Asia between years 2005 and 2016. *Environmental Research Letters*, *13*. https://doi.org/10.1088/1748-9326/aab2b3

Zheng, B., Chevallier, F., Yin, Y., Ciais, P., Fortems-Cheiney, A., Deeter, M. N., & Zhao, Y. (2019). Global atmospheric carbon monoxide budget 2000–2017 inferred from multi-species atmospheric inversions. *Earth System Science Data*, *11*. https://doi.org/10.5194/essd-2019-61

Zheng, B., Tong, D., Li, M., Liu, F., Hong, C., Geng, G., et al. (2018). Trends in China's anthropogenic emissions since 2010 as the consequence of clean air actions. *Atmospheric Chemistry and Physics*, *18*(19), 14,095–14,111. https://doi.org/10.5194/acp-18-14095-2018

Zheng, B., Tong, D., Li, M., Liu, F., Hong, C., Geng, G., & Zhang, Q. (2018). Trends in China's anthropogenic emissions since 2010 as the consequence of clean air actions. *Atmospheric Chemistry and Physics*, *18*. https://doi.org/10.5194/acp-18-14095-2018

Zhu, L., Jacob, D. J., Kim, P. S., Fisher, J. A., Yu, K., Travis, K. R., et al. (2016). Observing atmospheric formaldehyde (HCHO) from space: validation and intercomparison of six retrievals from four satellites (OMI, GOME2A, GOME2B, OMPS) with SEAC4RS aircraft observations over the southeast US. *Atmospheric Chemistry and Physics*, *16*(21), 13,477–13,490. https://doi.org/10.5194/acp-16-13477-2016